Received 7 June 2024; accepted 20 June 2024. Date of publication 24 June 2024; date of current version 19 July 2024.
Digital Object Identifier 10.1109/OJCOMS.2024.3418339

Massive MIMO for Aerial Highways: Enhancing Cell Selection via SSB Beams Optimization

MATTEO BERNABÈ [1,2] (Student Member, IEEE), DAVID LÓPEZ-PÉREZ [3] (Senior Member, IEEE), NICOLA PIOVESAN [1] (Member, IEEE), GIOVANNI GERACI [4,5] (Senior Member, IEEE), AND DAVID GESBERT [2] (Fellow, IEEE)

[1] Paris Research Center, Huawei Technologies, 92100 Boulogne-Billancourt, France
[2] Communications Systems Department, EURECOM, 06904 Sophia Antipolis, France
[3] ITEM Research Institute, Universitat Politècnica de València, 46022 Valencia, Spain
[4] Telefónica Research, Barcelona, Spain
[5] Department of Engineering, Universitat Pompeu Fabra, 08002 Barcelona, Spain

CORRESPONDING AUTHORS: M. BERNABÈ, D. LÓPEZ-PÉREZ, N. PIOVESAN, G. GERACI, and D. GESBERT (e-mail: matteo.bernabe@huawei.com; d.lopez@iteam.upv.es; nicola.piovesan@huawei.com; giovanni.geraci@upf.edu; david.gesbert@eurecom.fr)

This work was supported in part by the Generalitat Valenciana, Spain, through CIDEGENT PlaGenT under Grant CIDEXG/2022/17 and Project iTENTE; in part by the Spanish State Research Agency under Grant PID2021-123999OB-I00, Grant CEX2021-001195-M, and Grant CNS2023-145384; in part by the UPF-Fractus Chair on Tech Transfer and 6G; and in part by the Spanish Ministry of Economic Affairs and Digital Transformation and the European Union NextGenerationEU.

ABSTRACT In this article, we introduce a novel approach for enhancing cellular connectivity for unmanned aerial vehicles (UAVs) on aerial highways via terrestrial 5G networks. Owing to their ability to navigate 3D space, UAVs may experience favourable channel gains across multiple network cells; thus, from a network operator's perspective, selecting serving cells that maximize UAV capacity is not straightforward. Merely considering conventional metrics like reference signal received power (RSRP) may lead to selecting cells that offer high power but are inefficient in multiplexing UAVs, leading to possible reduced data rate performance. To tackle this problem, we propose a novel 5G synchronization signal block (SSB) beams planning solution to strategically control the UAVs cell association and maximize UAVs capacity without affecting terrestrial users. To solve the associated NP-hard problem, we propose a heuristic solution based on a novel metric that captures the multiplexing capability, average channel quality gain, and interference. Leveraging our proposed metric, we first optimally split the aerial highway and define serving cells, and then optimally select SSB beams and their transmitting power to ensure coverage from the previously defined serving cells set. Results indicate that our solution significantly improves the UAV data rate performance on aerial highways across different network scenarios and traffic conditions without impacting terrestrial users.

INDEX TERMS 3D network, 5G, SSB beam planning, UAV, aerial highways, cell association, drone corridors, mMIMO.

I. INTRODUCTION

WHAT will the future look like? The emergence of drones, also known as unmanned aerial vehicles (UAVs), has been foretold by experts and enthusiasts alike, envisioning a future where these flying marvels become an integral part of our society. This is no longer a distant vision, but a tangible reality. Fueled by their cost-effectiveness, and a remarkable ability to operate seamlessly in diverse and challenging conditions, drones have gathered significant attention [1], [2], [3], [4], [5], [6], [7], [8], [9], [10]. To quantify their ascending trajectory, recent reports have projected the value of the civil drone market at 5.1 billion U.S. dollars by 2028 [11]. Although success depends on efficiently providing well-defined services, such as imaging, agriculture, and search & rescue [12], urban environments pose a unique challenge, attracting only a few ventures so far. Amazon stands out as a pioneering force, launching its groundbreaking last-mile delivery service—Amazon Prime Air—in California in June 2022 [13]. Notably, Amazon's strategic move to extend this service to Italy and the United Kingdom by the end of 2024 [14], [15] signals a shift towards conquering urban spaces Building upon this burgeoning interest in UAVs within urban landscapes, the growth in drone utilization within human-inhabited spaces poses a critical challenge: developing regulations for optimal management and safety in urban skies. To tackle this concern, regulatory bodies and industries are collaboratively working to establish what can be deemed as the "highways of the sky" or simply aerial highways (AHs). Analogous to terrestrial highways, these designated airspace zones are poised to play a pivotal role in drone transportation, providing predefined routes for UAV flights [16]. In this context, communication coverage will not be the primary design principle. Instead, regulators will focus on making the routes efficient, safe, and conducive to both human and business needs. Communication issues will be addressed at a later stage once AHs are established. So, as traffic controllers plan AHs in accordance with specific and varying regulations for UAVs flights, network operators aiming to support beyond visual line of sight (BVLoS) services must adapt and optimize their networks to ensure reliable connectivity along these designated flight zones.

The high-speed, low-latency capabilities of 5G make it a prime contender to support the dynamic and data-intensive needs of AHs, ensuring seamless and efficient communication for urban drone navigation BVLoS [17], [18], [19], [20], [21]. However, 5G networks are optimized to serve ground user equipments (gUEs), and thus providing service to UAVs in general, and AHs in particular, comes with a series of significant challenges. Overall, the radio propagation characteristics for UAVs differ significantly from conventional gUEs. Operating at considerable altitudes above the clutter of human-made structures inherently leads to favorable line of sight (LoS) conditions across potentially many cells.[1] This unique scenario may result in UAVs receiving comparable signal power from multiple cells, introducing complexities in determining the optimal serving cell, and potentially disruptive interference for both downlink and uplink transmissions. As most networks operate multiple-input multiple-output (MIMO) today, the high spatio-temporal correlation among the complex channels of nearby UAVs in an AH may also significantly affect the overall drone performance [22], [23], [24], [25], [26].

A. RELATED WORK

To address the intricate challenges of navigating UAVs in diverse environments, the research community has primarily focused on optimizing decisions and actions on the UAV side. Two notable solution categories have emerged. Generally speaking, the first involves UAV trajectory planning that maximizes UAV coverage, and/or rate, while simultaneously minimizing the impact on gUE performance due to resource sharing [27], [28], [29], [30], [31]. The second explores methods to enhance the robustness of UAV communications, primarily through optimal UAV association and multi-connectivity, optimizing the selection of serving cells and/or some of their transmit characteristics [32], [33], [34]. Yet, these autonomous, network-aware decision-making processes do not account for the challenges posed by AHs, and may lead to extended travel times, increased onboard complexity, and higher energy consumption. Additionally, the scalability of autonomous navigation plans is challenged by the increasing UAVs number, potentially conflicting with forthcoming safety regulations.

From our perspective, AHs demand a distinct approach. Rather than adapting UAV behaviours, AHs require optimizing existing or to-be-deployed networks to meet the UAVs' unique needs. However, research in this direction remains limited. The work in [35] marked a milestone by investigating the optimal number and positions of millimetre wave (mmWave) base stations with up-tilted antenna arrays required to serve AHs in an urban environment. Building upon this, the authors of [36] extended the exploration, analyzing the benefits of non-orthogonal multiple access (NOMA) for uplink transmissions in drone corridors. Focusing on the sub-6 GHz band, the study in [37] examined the advantages of deploying additional uptilted base stations AHs. Importantly, they provided an analytical framework to assess outages in an AH under specific assumptions. In the context of 4G networks, breaking new ground in [38], researchers pioneered a novel approach to tackle the intricacies of practical networks serving AHs. Instead of emphasizing the deployment of new uptilted infrastructure, they introduced a sophisticated mathematical framework based on quantization theory to optimize the downlink signal-to-interference-plus-noise ratio (SINR) for both terrestrial and aerial user equipments (UEs). This optimization involved fine-tuning the downtilt and transmit power of already deployed base stations. With a similar motivation, the authors of [39] recently introduced a methodology based on machine learning (ML) and bayesan optimization (BO) for adjusting the sectors' electrical tilt and power, learning form the environment, with the final goal of maximizing the downlink SINR for both terrestrial and aerial UEs. Generalization aspects of the learnt model were studied too. Despite these contributions, it is crucial to highlight that none addressed the complex challenges of operating 5G networks for AHs, particularly in the context of prevalent massive multiple-input multiple-output (mMIMO) technology.

B. OPEN PROBLEMS AND OUR CONTRIBUTION

Given its powerful precoding capabilities, mMIMO has become a key physical layer technology for 5G, and is

[1] In this work, the terms "cell" and "sector" are used interchangeably.

expected to remain a cornerstone technology into the 6G era. In recent years, several studies have underscored the advantages of mMIMO in enhancing UAVs connectivity [40], [41], [42]. Notably, beamforming has proven to be especially valuable in managing interference to and from UAVs, while spatial multiplexing capabilities have played a pivotal role in enhancing UEs data rates. However, these studies have largely focused on scenarios involving sparsely located, hovering UAVs, overlooking the complexities of UAVs operating in dense, dynamic environments like AHs.

As UAVs traffic in AHs increases, the close proximity of UAVs and the dominance of LoS channel condition, lead to higher channel correlation, posing significant challenges for mMIMO systems. We identify two critical research gaps: the lack of research on optimal UAVs cell associations under practical mMIMO configurations, and a scarcity of studies on large-scale downlink mMIMO optimization in 5G sub-6 GHz networks, especially in scenarios incorporating UAVs and AHs. Therefore, in this work, we propose a novel solution that leverages the knowledge of the AH to optimally plan 5G synchronization signal block (SSB) beams. This strategy aims to control UAVs cell associations to maximise their capacity along the AH without impacting terrestrial users.

It should be noted that, in contrast with the related studies referenced previously, this work presents the following distinctive characteristics: *i)* it explores solutions within terrestrial networks rather than focusing on UAVs actions, such as trajectory planning and transmission schemes. As a result, it does not introduce additional complexity or payload on-board, which is crucial for UAVs efficiency and security. *ii)* Unlike works that rely on UAVs supported by dedicated terrestrial infrastructure, this study focuses on reusing existing networks. This approach minimizes the need to invest in additional high-cost dedicated infrastructure. *iii)* While existing literature on the optimization of already deployed networks for UAVs often focuses on reusing 4G infrastructure, this work targets 5G mMIMO scenarios, which are characterized by high complexity and significant interplay among numerous system parameters. *iv)* While literature has established mMIMO as a pivotal technology for enhancing aerial communications, those studies typically focus on a few sparsely located UAVs within the network. In contrast, this work is grounded in the forthcoming regulations that will govern air traffic through AHs. It considers several UAVs densely packed in a small area (i.e., AH) and addresses the resultant challenges, including the high channel correlation due to typical LoS conditions, which severely limits spatial multiplexing capabilities. *v)* This work focuses solely on optimizing the UAVs cell association to enhance connectivity through the optimal panning of the coverage SSBs beams. This has never been attempted before to the best of our knowledge. *vi)* Moreover, this work is also the first to present a scalar metric for defining the set of serving cells aimed at serving the AH, and *vii)* design a two-stage evolutionary algorithm that combines particle swarm optimization (PSO) and an elite genetic algorithm (eGA) to optimally segment the AH, identify the set of serving cells for each AH‘segment, and determine the optimal configuration of coverage SSB beams. *viii)* Finally, but most significantly, this work operates under realistic and practical assumptions. Importantly, to avoid potential cell re-selection and handover issues, we do not aim to optimize coverage in real-time to meet instantaneous communication needs. Instead, with the final goal of enhancing the UAVs data rate, we focus on providing the best stable coverage over precise segments of the AH, using the set of optimal serving cells identified by the introduced novel metric.

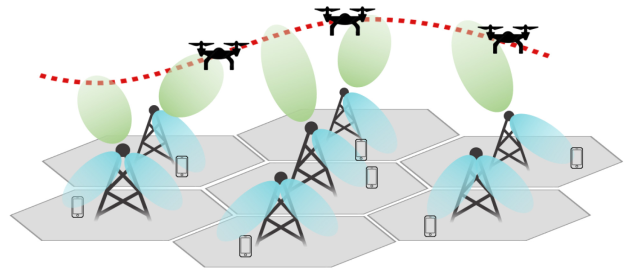

FIGURE 1. **Ilustration of an aerial highway and flying UAVs covered by SSBs beams from a terrestrial network.**

Our contribution can be summarized as follows:

- We formulate an optimization problem to select optimal coverage beams, along with their transmit power for each cell throughout the network. This strategy aims to maximize UAV data rates while minimizing the impact on gUEs, under practical constraints such as transmit power limitations and SSB beams planning restrictions. Additionally, we prioritize minimizing the number of varied SSB beams for each cell during the optimization process.
- We introduce a novel metric for optimally identifying AH serving cells, considering multiplexing capability, average channel gain, and cell interference. This metric leverages the existing knowledge on the predefined path of AHs enabling efficient serving cell selection. This metric extends our previous work presented in [43].
- Leveraging the proposed metric, we formulate a two-stage heuristic solution to tackle the SSB beams planning problem. First, we define a problem and a PSO-based algorithm to solve the non-convex problem and split the AH while determining the set of serving cells. Then, we formulate a problem to determine the optimal SSB beams and transmit power for these serving cells. To solve the resulting mixed-integer non-convex problem, we design a genetic algorithm (GA) solution.
- Through extensive simulation results, we demonstrate that our solution achieves gains up to 5.15 dB and 550% for the 5%-tile of UAVs SINR and achievable data rate, respectively, with almost null impact on terrestrial performance.

The remainder of this paper is organized as follows. Section II introduces the system model used in our study. Section III presents the constrained optimization problem for the SSB beam optimal planning aimed at maximizing UAV achievable rates while minimizing impact on the terrestrial network. Section IV motivates and introduces a novel metric for selecting serving cells for AHs, Section V, leveraging the designed metric, details the two-stage algorithm solution to solve the optimization problem efficiently. Section VI presents simulation results that demonstrate the efficacy of our approach. Finally, we conclude the paper in Section VII.

II. SYSTEM MODEL

In this section, we introduce the models adopted in our analysis. In particular, we consider a cellular network operating in the sub-6 GHz spectrum (FR1) with carrier frequency f_c and full frequency reuse. The adopted models adhere to the stochastic 3rd Generation Partnership Project (3GPP) modelling assumptions outlined in [44], [45].

1) NETWORK CELLS DEPLOYMENT

In our system-level analysis, we consider an outdoor urban network which comprises 19 base station sites arranged in a 2-tier hexagonal grid, with an inter-site distance d_{ISD}. Each site has a height h_{BS}, and hosts 3 sectors. The cells' boresight orientations are evenly spaced by 120°, ensuring consistent orientations across the network. The set of all cells is represented as $\mathcal{B}$, and its cardinality is denoted by N_{BS}.

2) SECTOR PANEL AND ANTENNA ELEMENT GAIN

Each sector $b \in \mathcal{B}$ is then equipped with a uniform planar array (UPA) antenna panel, consisting of M_h horizontal and M_v vertical single vertical polarized antenna element, totaling $M = M_h \times M_v$ elements. The spacing between antenna elements is $\lambda_p/2$, where λ_p is the panel wavelength, designed according to the operating frequency f_c.

In the following, we present models outlined by 3GPP in [44] for the single antenna element gain between each UE u and cell b, here denoted as $g_{u,b}$. Specifically, it is computed as follows,

$$g_{u,b} = G_0 - \min\left(-\left(G^H_{u,b} + G^V_{u,b}\right), 30\right) \tag{1}$$

where

$$G^H_{u,b} = -\min\left(12\left(\frac{\phi_{u,b}}{\phi_{3\text{dB}}}\right)^2, 30\right) \tag{2}$$

$$G^V_{u,b} = -\min\left(12\left(\frac{\theta_{u,b} - \theta_{\text{tilt}}}{\theta_{3\text{dB}}}\right)^2, 30\right). \tag{3}$$

where $\phi_{u,b}$ and $\theta_{u,b}$ are the relative azimuth and zenith angles between UE u and cell b, in degrees. Moreover, the zenith angle $\theta_{u,b}$=0 points toward the sky, angles $\phi_{3\text{dB}}$, $\theta_{3\text{dB}}$ are equally set to 65° and θ_{tilt} is the vertical tilt of the sector set to 105°. Finally, G_0 is the maximum directional gain set to 8 dBi [44].

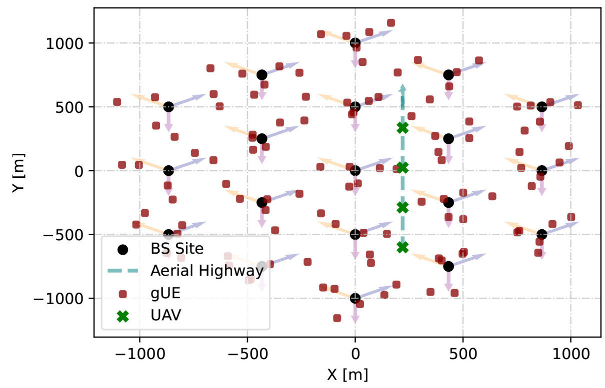

FIGURE 2. 2D network layout with random gUEs and example of aerial highways with UAVs.

3) USER DEPLOYMENT

In this work, we assume a fully loaded scenario with a total number of N_u single-antenna UEs. We consider N_g outdoor gUEs uniformly randomly distributed with each cell of the network and N_a UAVs located over an aerial highway that stretches over several cell centres and edges at altitude h_{AH}. Along the AH, all UAVs are evenly spaced with a fixed inter-UAV distance d_{IUD}.

To reflect the dynamic characteristics of real scenarios, while all UAVs move along the AH, the gUEs location randomly changes with time. Then, to maintain a continuous traffic condition, when a UAV exits, a new one enters.

Figure 2 depicts an example of the 2D network layout with randomly deployed UEs and UAVs located on a AH.

A. CHANNEL MODEL

To assess signal quality, we utilize the statistical channel model outlined by the 3GPP in [44] and its extension to aerial scenarios in [45]. These models are employed to calculate various channel features between each UE $u \in \mathcal{U}$ and cell $b \in \mathcal{B}$, such as LoS probability $P^{\text{LoS}}_{u,b}$, path loss gain $\rho^{\text{LoS}}_{u,b}$, shadow fading gain $\tau^{\text{LoS}}_{u,b}$ and small-scale fading downlink channel vectors $\mathbf{h}^{\text{dl}}_{u,b}$.

To account for varying environmental conditions, we consider a total of N_{real} realizations for the UEs positions and their stochastic downlink channels realization.

1) LOS PROBABILITY AND PATH LOSS GAIN

To compute the LoS probability $P^{\text{LoS}}_{u,b}$ and the path loss gain $\rho^{\text{LoS}}_{u,b}$ for each u and each cell b, this work adopts the models outlined by 3GPP in [44], [45]. Specifically, the employed models consider both urban macro (UMa) and urban micro (UMi) scenarios and differentiate between gUEs located on the ground segment and UAVs located on the aerial one. A detailed description of these models is provided in the Appendix of this manuscript.

2) SHADOW FADING GAIN

In this work, we model the stochastic shadow fading gain $\tau_{u,b}$, between each UE u and cell b, as a zero mean

TABLE 1. Summary of shadow fading standard deviation.

UMa				UMi			
Ground		Aerial		Ground		Aerial	
LoS	NLoS	LoS	NLoS	LoS	NLoS	LoS	NLoS
4	6	eq. (4)	6	4	7.82	eq. (5)	8

log-normal random variable, with standard deviation values outlined by 3GPP in [44], [45]. As described in [45], for aerials, standard deviation values under LoS conditions depend on the altitude. Specifically, those values are computed as,

$$\sigma_{\text{SF}}^{\text{UAV-UMa-LoS}} = 4.64e^{-0.0066 h_{\text{AH}}}, \tag{4}$$

$$\sigma_{\text{SF}}^{\text{UAV-UMi-LoS}} = \max\left(5e^{-0.01 h_{\text{AH}}}, 2\right). \tag{5}$$

The standard deviation values in dB are summarized in Table 1.

Moreover, following the work presented in [46], we incorporate 2D spatial correlation within the log-normal shadow fading.

3) MULTI-PATH FADING

In the following, we introduce the small-scale fading capturing the multi-path nature of the link between each UE u and the M antennas of each sector b. Specifically, we model the small-scale fading as a Rician fading. Embracing the plane wave approximation [44], [47], the resulting downlink small-scale channel $\mathbf{h}_{u,b}^{\text{dl}} \in \mathbb{C}^{1\times M}$ is modeled as follows:

$$\mathbf{h}_{u,b}^{\text{dl}} = \sqrt{\frac{K}{1+K}}\,\mathbf{h}_{u,b}^{\text{LoS}} + \sqrt{\frac{1}{1+K}}\,\mathbf{h}_{u,b}^{\text{NLoS}}, \tag{6}$$

with

$$\mathbf{h}_{u,b}^{\text{LoS}} = e^{-j\frac{2\pi}{\lambda_c} d_{u,b}^{\text{3D}}}\, e^{j\frac{2\pi}{\lambda_c}\,\mathbf{k}_{u,b}^{T}(\phi_{u,b},\theta_{u,b})\,\mathbf{V}_b} \tag{7}$$

and

$$\mathbf{h}_{u,b}^{\text{NLoS}} \sim \mathbb{CN}(\mathbf{0}, \mathbf{I}_M), \tag{8}$$

where we recall $d_{u,b}^{\text{3D}}$ is the 3D distance between UE u and the center of sector b's antenna array, then, $\phi_{u,b}$ and $\theta_{u,b}$ are their relative azimuth and zenith angles, respectively, and K is the Rician factor. The wave vector $\mathbf{k}_{u,b}(\cdot,\cdot)$ represents the phase variation of a plane wave in 3D-orthogonal directions, defined as follows:

$$\mathbf{k}_{u,b}\left(\phi_{u,b}, \theta_{u,b}\right) = \begin{bmatrix} \cos\left(\phi_{u,b}\right)\cos\left(\theta_{u,b}\right) \\ \sin\left(\phi_{u,b}\right)\cos\left(\theta_{u,b}\right) \\ \sin\left(\theta_{u,b}\right) \end{bmatrix}, \tag{9}$$

and $\mathbf{V}_b$ is the matrix containing the Cartesian coordinates of each antenna element w.r.t. the panel centre, given by

$$\mathbf{V}_b = \begin{bmatrix} \mathbf{v}_b^x \\ \mathbf{v}_b^y \\ \mathbf{v}_b^z \end{bmatrix} = \begin{bmatrix} v_{0,b}^x, & \dots, & v_{m,b}^x, & \dots, & v_{M-1,b}^x \\ v_{0,b}^y, & \dots, & v_{m,b}^y, & \dots, & v_{M-1,b}^y \\ v_{0,b}^z, & \dots, & v_{m,b}^z, & \dots, & v_{M-1,b}^z \end{bmatrix}. \tag{10}$$

B. CELL ASSOCIATION

In the initial phase of cell discovery and association, each sector b transmits beamformed signals in various spatial directions to optimally cover the assigned area. Within each beam, the so-called SSBs are transmitted, consisting of the primary synchronization signal (PSS), secondary synchronization signal (SSS), and physical broadcasted channel (PBCH). This allows a UE to synchronize with the network, conduct measurements, and select the serving cell. In the sub-6 GHz band, as specified by 3GPP standards [48], [49], each sector is constrained to transmit a maximum of N_{ssb} SSBs beams. Additionally, each sector performs SSB beam sweeping: a procedure where all beams, each with index i^{ssb}, are transmitted sequentially according to a sweeping pattern.

Each SSB beam s of the N_{ssb} SSB beams in a sector b is generated using a specific codeword $\mathbf{w}_{s,b}^{\text{ssb}} \in \mathbb{C}^{M\times 1}$ selected from a predefined codebook $\mathbf{W}^{\text{ssb}} \in \mathbb{C}^{M\times N_{\text{CB}}}$. This codebook is composed of N_{CB} codewords. In this work, the SSB codebook $\mathbf{W}^{\text{ssb}}$ is generated via two dimensional discrete Fourier transform (2D-DFT) precoding, an approach widely used in the field.

To determine its serving cell $\hat{b}_u$, each UE u first computes the reference signal received power (RSRP) from each SSB beam s of each sector b as follows:

$$\begin{aligned} \text{rsrp}_{u,s,b}^{\text{ssb}} &= \beta_{u,b}\left|\mathbf{h}_{u,b}^{\text{dl}}\,\mathbf{w}_{s,b}^{\text{ssb}}\right|^2 p_{s,b}^{\text{ssb}} \\ &= \rho_{u,b}\,\tau_{u,b}\,g_{u,b}\left|\mathbf{h}_{u,b}^{\text{dl}}\,\mathbf{w}_{s,b}^{\text{ssb}}\right|^2 p_{s,b}^{\text{ssb}}, \end{aligned} \tag{11}$$

where $\beta_{u,b}$ denotes the large-scale channel gain and $p_{s,b}^{\text{ssb}}$ is the transmit power of the considered SSB beam. Subsequently, the serving SSB beam $\hat{s}_u$, and in turn the serving cell $\hat{b}_u$ are derived as follows:

$$\hat{s}_u, \hat{b}_u = \arg\max_{s,b}\left\{x_{s,b}\,\beta_{u,b}\left|\mathbf{h}_{u,b}^{\text{dl}}\,\mathbf{w}_{s,b}^{\text{ssb}}\right|^2 p_{s,b}^{\text{ssb}}\right\}, \tag{12}$$

with $x_{s,b} \in \mathbf{X}$, where the binary matrix $\mathbf{X} \in \{0,1\}^{N_{CB}\times N_{BS}}$ represent the set of deployed SSB beams within the network, i.e., if $x_{s,b}$ equals 1, beam s is deployed in cell b. To evaluate SSB beam coverage, we compute the SINR γ_u^{ssb} experienced by UE u from the chosen serving cell b and SSB beam $\hat{s}_u$ as follows:

$$\gamma_u^{\text{ssb}} = \frac{\text{rsrp}_{u,\hat{s}_u,\hat{b}_u}^{\text{ssb}}}{\sum_{b\in\mathcal{B}\setminus\hat{b}_u}\sum_{s}^{N_{\text{CB}}} x_{s,b}\,\text{rsrp}_{u,s,b}^{\text{ssb}}\,\delta\left(i_{\hat{s}_u}^{\text{ssb}}, i_s^{\text{ssb}}\right) + B_0 N_0}, \tag{13}$$

with

$$\delta(i,j) = \begin{cases} 1, & \text{If } i=j \\ 0, & \text{Otherwise} \end{cases}. \tag{14}$$

As a result of the temporal beam sweeping mechanism, only beams associated with the same index i^{ssb} interfere with one another. Thus, within the aforementioned formulation, $\delta(\cdot,\cdot)$ is the Kronecker delta function computed for the pair of SSB beam indices. Finally, N_0 is the thermal noise spectral density.

C. DATA PRECODING

To harness mMIMO beamforming and multiplexing capabilities, this work adopts a Type I channel state information-reference signal (CSI-RS)-based operation, specifically designed for high-mobility scenarios [50], [51]. Without loss of generality, our focus is on multi-user massive multiple-input multiple-output (MU-mMIMO) with a single-layer transmission per UE. In this mode of operation, the cell configures multiple CSI-RS beams, and instructs each UE to report a set of indices, characterizing the channel conditions, via a Type I channel state information (CSI) report. More in detail, each transmitted CSI-RS beam is precoded with a codeword selected from a 2D-DFT CSI-RS codebook $\mathbf{W}_b^{\text{csi-rs}}$, enabling each cell to transmit up to 32 distinct CSI-RS beams simultaneously, in accordance with 3GPP standards [49], [51]. UEs are then instructed to measure the received power from each of those and then to report indices to the serving cell, including the rank indicator (RI), precoding matrix indicator (PMI), and channel quality indicator (CQI), encapsulated within the Type I CSI report. Through the PMI, UEs report the index of the codeword $\mathbf{w}_{\text{pmi}}^{\text{csi-rs}}$ from the codebook $\mathbf{W}_b^{\text{csi}-\text{rs}}$ that provided the highest received power, i.e., the largest CSI-RS RSRP. The cell then uses this UE-reported codeword $\mathbf{w}_{\text{pmi}}^{\text{csi-rs}}$ as the transmit precoder $\mathbf{w}_{u,\hat{b}_u}^{\text{dl}}$ on the data channel [49], [50], [51].

It should be noted that within this configuration, each UE does not estimate and reports back channel coefficients, but indeed only indexes regarding the measured CSI-RS beam received power; therefore accounting for robustness against errors in the channel estimation.

According to the above, the data precoding vector for a UE u served by cell $\hat{b}_u$ can then be formulated as follows:

$$\mathbf{w}_{u,\hat{b}_u}^{\text{dl}} = \mathbf{w}_{\text{pmi}}^{\text{csi-rs}} = \arg \max_{\mathbf{w}_{\text{pmi}}^{\text{csi-rs}} \in \mathbf{W}_{\hat{b}_u}^{\text{csi-rs}}} \left\{ \beta_{u,\hat{b}_u} \left| \mathbf{h}_{u,\hat{b}_u}^{\text{dl}} \, \mathbf{w}_{\text{pmi}}^{\text{csi-rs}} \right|^2 \right\}. \tag{15}$$

Finally, for each cell b we define the $\mathbf{W}_b^{\text{dl}}$ as the set of all different precoders adopted to serve its set of connected users.

D. SINR AND ACHIEVABLE DATA RATE

The received signal y_u for each UE u can be expressed as:

$$\begin{aligned} y_u = {} & \sqrt{\beta_{u,\hat{b}_u}} \, \mathbf{h}_{u,\hat{b}_u}^{\text{dl}} \, \mathbf{w}_{u,\hat{b}_u}^{\text{dl}} \sqrt{p_{u,\hat{b}_u}^{\text{dl}}} \\ & + \sqrt{\beta_{u,\hat{b}_u}} \sum_{p \in \mathcal{U}_{\hat{b}_u} \setminus u} \left(1 - \delta\left(\mathbf{w}_{u,\hat{b}_u}^{\text{dl}}, \mathbf{w}_{p,\hat{b}_u}^{\text{dl}}\right)\right) \mathbf{h}_{u,\hat{b}_u}^{\text{dl}} \, \mathbf{w}_{p,\hat{b}_u}^{\text{dl}} \sqrt{p_{p,\hat{b}_u}^{\text{dl}}} \\ & + \sum_{b \in B \setminus \hat{b}_u} \sqrt{\beta_{u,b}} \sum_{\mathbf{w}_{i,b}^{\text{dl}} \in \mathbf{W}_b^{\text{dl}}} \frac{1}{N_{\mathbf{w}_{i,b}^{\text{dl}}}} \, \mathbf{h}_{u,b}^{\text{dl}} \, \mathbf{w}_{i,b}^{\text{dl}} \sqrt{p_{i,b}^{\text{dl}}} \; + \; n_u, \end{aligned} \tag{16}$$

where $\mathcal{U}_{\hat{b}_u} \subseteq \mathcal{U}$ denotes the subset of UEs connected to sector $\hat{b}_u$, $\mathbf{w}_{u,b}^{\text{dl}} \in \mathbb{C}^{M \times 1}$ and $p_{u,b}^{\text{dl}}$ are the downlink precoding vector and transmit power used at sector b to serve UE u, respectively, and n_u is the thermal noise. In this work, we consider equal power transmission for all UEs. Furthermore, when a pair of UEs, denoted as u and p, select identical precoding codewords, the cell ensures orthogonal service by allocating distinct physical resource blocks (PRBs) to them. Thus, the Kronecker delta function $\delta(\cdot, \cdot)$ reflects this network characteristic in the computation of the intra-cell interference.

The resulting SINR γ_u for each UE u is given by eq. (17), as shown at the bottom of the page, where, $N_{\text{PRB}}^{\text{tot}}$ is the total number of PRBs available, B_{PRB} denotes the bandwidth of each PRB, $N_{\mathbf{w}_{u,\hat{b}_u}^{\text{dl}}}$ is the number of UEs within the same cell that are served by the same beam/precoder $\mathbf{w}_{u,\hat{b}_u}^{\text{dl}}$ as UE u, and, finally, N_0 is the thermal noise spectral density power.

Assuming an equal long-term resource share among UEs, as typically done in round-robin schedulers, the achievable data rate R_u for each UE u is obtained as follows:

$$R_u = \frac{N_{\text{PRB}}^{\text{tot}} \, B_{\text{PRB}}}{N_{\mathbf{w}_{u,\hat{b}_u}^{\text{dl}}}} \, \log_2(1 + \gamma_u). \tag{18}$$

III. PROBLEM FORMULATION

Optimizing large-scale sub-6 GHz mMIMO networks presents significant complexity within the context of AHs, as previously introduced. Our hypothesis suggests that the data rate achievable by UAVs operating within AHs can be significantly enhanced by optimally managing the UAVs' cell associations alone. The foremost benefit of this strategy lies in its feasibility, focusing exclusively on optimising the SSB beams planning strategy to enhance overall UAV performance.

In this section, we formulate an optimization problem to strategically plan SSB beams, therefore managing UAV cell associations along AHs. This involves optimizing the selection and transmit power of SSBs beams that dictate network UE cell associations, aiming to enhance UAV data rates while ensuring no negative impact on gUEs. Moreover, following the realistic constraints of network operators—who often resist extensive network changes due to the potential deviation from well-performing configurations, management cost concerns, or general risk aversion—we account for the number of changes applied to the network, specifically focusing on the number of varied SSB coverage beams.

The overall problem is formulated in what follows.

$$\gamma_u = \frac{\beta_{u,\hat{b}_u} \left| \mathbf{h}_{u,\hat{b}_u}^{\text{dl}} \, \mathbf{w}_{u,\hat{b}_u}^{\text{dl}} \right|^2 p_{u,\hat{b}_u}^{\text{dl}}}{\beta_{u,\hat{b}_u} \sum_{p \in \mathcal{U}_{\hat{b}_u} \setminus u} \left(1 - \delta\left(\mathbf{w}_{u,\hat{b}_u}^{\text{dl}}, \mathbf{w}_{p,\hat{b}_u}^{\text{dl}}\right)\right) \left| \mathbf{h}_{u,\hat{b}_u}^{\text{dl}} \, \mathbf{w}_{p,\hat{b}_u}^{\text{dl}} \right|^2 p_{p,\hat{b}_u}^{\text{dl}} + \sum_{b \in B \setminus \hat{b}_u} \beta_{u,b} \sum_{\mathbf{w}_{i,b}^{\text{dl}} \in \mathbf{W}_b^{\text{dl}}} \frac{1}{N_{\mathbf{w}_{i,b}^{\text{dl}}}} \left| \mathbf{h}_{u,b}^{\text{dl}} \, \mathbf{w}_{i,b}^{\text{dl}} \right|^2 p_{i,b}^{\text{dl}} + \frac{N_{\text{PRB}}^{\text{tot}} \, B_{\text{PRB}}}{N_{\mathbf{w}_{u,\hat{b}_u}^{\text{dl}}}} N_0} \tag{17}$$

Problem 1: SSB Beams Planning Optimization

$$\min_{\mathbf{X},\mathbf{P}} \; f_a\Big(\hat{\mathbf{b}}(\mathbf{X},\mathbf{P})\Big) - g_g\Big(\hat{\mathbf{b}}(\mathbf{X},\mathbf{P}), \hat{\mathbf{b}}\Big(\mathbf{X}^{\text{bl}},\mathbf{P}^{\text{bl}}\Big)\Big) - k\Big(\mathbf{X},\mathbf{X}^{\text{bl}}\Big)$$

$$\text{s.t.} \; \sum_{s}^{N_{CB}} x_{s,b} = N_{\text{ssb}}, \; \forall b \in \mathcal{B} \qquad (C1.1)$$

$$\frac{1}{2}\sum_{s}^{N_{CB}}\Big(1 - x_{s,b}\, x^{\text{bl}}_{s,b}\Big) \leq N'_{\text{ssb}}, \; \forall b \in \mathcal{B} \qquad (C1.2)$$

$$0 \leq p^{\text{ssb}}_{s,b} \leq p^{\text{ssb}}_{\max}, \;\; \forall p^{\text{ssb}}_{s,b} \in \mathbf{P} \qquad (C1.3)$$

$$\mathbf{X} \in \{0,1\}^{N_{CB}\times N_{BS}} \qquad (C1.4)$$

$$\mathbf{P} \in \mathbb{R}^{N_{CB}\times N_{BS}} \qquad (C1.5)$$

with

$$f_a\Big(\hat{\mathbf{b}}(\mathbf{X},\mathbf{P})\Big) = \mathbb{E}_{\tau,\mathbf{h}^{\text{dl}}}\left\{\log\left(\sum_{a}^{N_a} R_a\Big(\hat{\mathbf{b}}(\mathbf{X},\mathbf{P})\Big)\right)\right\}, \qquad (19)$$

$$g_g\Big(\hat{\mathbf{b}}(\mathbf{X},\mathbf{P}), \hat{\mathbf{b}}\Big(\mathbf{X}^{\text{bl}},\mathbf{P}^{\text{bl}}\Big)\Big) = \mathbb{E}_{\tau,\mathbf{h}^{\text{dl}}}\left\{\sum_{g}^{N_g}\left|R_g\Big(\hat{\mathbf{b}}(\mathbf{X},\mathbf{P})\Big) - R_g\Big(\hat{\mathbf{b}}\Big(\mathbf{X}^{\text{bl}},\mathbf{P}^{\text{bl}}\Big)\Big)\right|\right\}, \qquad (20)$$

and

$$k\Big(\mathbf{X},\mathbf{X}^{\text{bl}}\Big) = \frac{1}{2}\,\mathbf{e}^T\Big(1 - \Big(\mathbf{X}\odot\mathbf{X}^{\text{bl}}\Big)\Big)\,\mathbf{e} = \frac{1}{2}\sum_{b}^{N_{BS}}\sum_{s}^{N_{CB}} 1 - x_{s,b}\, x^{\text{bl}}_{s,b}\,, \qquad (21)$$

with the binary matrix $\mathbf{X}$, introduced in Section II, directly affecting UEs' cell associations as detailed in eq. (12). Specifically, an element $x_{s,b}$ within matrix $\mathbf{X}$ equaling one indicates the selection of the s-th SSB beam at cell b. Correspondingly, an element $p^{\text{ssb}}_{b,s}$ within matrix $\mathbf{P}$ indicates the transmit power allocated by cell b to the s-th SSB beam. Additionally, matrices $\mathbf{X}^{\text{bl}}$ and $\mathbf{P}^{\text{bl}}$ represent the SSB configuration before the optimization process begins, i.e., in an scenario with no UAVs. We refer to this scenario as the baseline (bl) one.

The objective function in Problem (1) comprises the following terms:

- $f_a(\cdot)$, defined in eq. (19) and leveraging the $\log(\cdot)$ function to calculate a fair sum rate across all UAVs, ensuring equitable UAV service.
- $g_g(\cdot,\cdot)$, defined in eq. (20) and evaluating the impact of UAV integration on gUE data rates through the optimization decisions made and represented in matrices $\mathbf{X}$ and $\mathbf{P}$, aiming to minimize disruption to existing services.
- $k(\cdot,\cdot)$, defined in eq. (21) and measuring optimization-induced changes to SSBs beams via the Hadamard product of $\mathbf{X}$ and $\mathbf{X}^{\text{bl}}$, with all element summation, adjusted by a factor of $1/2$, to reflect the change count. Note that in eq. (21) $\mathbf{e}$ is a vector of all ones.

Data rates in eqs. (19) and (20) are calculated according to eq. (18).

Feasible solutions to Problem (1) must meet the following constraints:

- C1.1, mandating each cell b to deploy N_{ssb} SSB beams.
- C1.2, limiting cell modifications to of N'_{ssb} SSB beams for adaptability without compromising stability.
- C1.3, controlling the transmit power per SSB beam.
- C1.4 and C1.5, defining $\mathbf{X}$ and $\mathbf{P}$ matrices space.

Problem (1), characterized by high dimensionality, inherent stochasticity, non-linearity, and the combinatorial nature of the mixed binary integer variables, represents an NP-hard problem. To tackle this problem, in Section IV we introduce a novel metric to optimally select aerial highway serving cells. Then, leveraging the proposed metric, in Section V we propose a heuristic solution which divides Problem (1) into two substantially less complex sub-problems and solves them.

IV. AERIAL HIGHWAY SERVING CELL

Utilizing mMIMO to serve closely located UAVs in an AH poses challenges, primarily due to the inherent high channel correlation. Channel correlation is intensified in the AH environment as UAVs fly in close proximity to each other, often with direct LoS. This diminishes spatial diversity, crucial for effective mMIMO operation, limiting the system's capacity for simultaneous transmission/reception of multiple data streams to/from different UAVs. The independent design of the AH with respect to the network can further exacerbate this challenge. For instance, consider a scenario where the AH is perpendicular to the mMIMO planar array of the sector providing the highest power. In such a case, the sector may be unable to resolve the highly-correlated spatial signatures of the UAVs flying along the AH, as they appear at approximately the same angle of arrival (AoA) and angle of departure (AoD). To address these challenges, it may prove advantageous to associate with a sector offering superior multiplexing capabilities at the expense of a slightly weaker signal.

To address this issue, we introduce a novel metric that aims to optimize the selection of the set of cells aimed to serve UAVs along the AH. The proposed metric leverages AH a-priori information, i.e., define trajectory, and channel state information measurements, and it accounts for received signal strength, spatial diversity, and potential interference.

A. AERIAL SEGMENT TO CELL ASSOCIATION METRIC

In order to define our proposed metric, we discretize the AH into N_r points $\mathbf{r}_{\text{AH}}$ with equal inter-point distance d_r to simplify the problem. Leveraging existing simulations and/or measurements collected during exploratory UAV flights in the planning phase, we derive the expected complex channel vector $\tilde{\mathbf{h}}_{r,b}$ between each of these N_r points and each cell b, as expressed by:

$$\tilde{\mathbf{h}}_{r,b} = \mathbb{E}_{\tau,\mathbf{h}^{\text{dl}}}\Big[\beta_{r,b}\,\mathbf{h}^{\text{dl}}_{r,b}\Big] = \mathbb{E}_{\tau,\mathbf{h}^{\text{dl}}}\Big[\rho_{r,b}\,\tau_{r,b}\,g_{r,b}\,\mathbf{h}^{\text{dl}}_{r,b}\Big]. \quad (22)$$

Subsequently, we utilize these vectors to construct the expected complex channel matrix $\tilde{\mathbf{H}}_{\mathbf{r},b} \in \mathbb{C}^{N_r\times M}$.

Furthermore, we define the segment $\mathbf{z}$ within the AH $\mathbf{r}_{\mathrm{AH}}$ as the set of consecutive discrete N_z points such that

$$\mathbf{z} \subset \mathbf{r}_{\mathrm{AH}} \quad \text{and,} \quad M < N_z < N_r. \tag{23}$$

Then, from matrix $\tilde{\mathbf{H}}_{\mathbf{r},b}$, we define two sub-matrices $\tilde{\mathbf{H}}_{\mathbf{z},b}$ and $\tilde{\mathbf{H}}_{\mathbf{r}-\mathbf{z},b}$, respectively denoting the complex channel vectors of segment $\mathbf{z}$ and of the remaining AH discrete points, such that,

$$\tilde{\mathbf{H}}_{\mathbf{z},b} \cup \tilde{\mathbf{H}}_{\mathbf{r}-\mathbf{z},b} = \tilde{\mathbf{H}}_{\mathbf{r},b}, \quad \tilde{\mathbf{H}}_{\mathbf{z},b} \cap \tilde{\mathbf{H}}_{\mathbf{r}-\mathbf{z},b} = \emptyset. \tag{24}$$

According to the above-defined channel matrices, we introduce our proposed metric, referred to as mMIMO-Aerial-Metric-Association (MAMA) aimed at addressing the limitations of the widely adopted best-RSRP association policy when dealing with AHs:

$$\chi_{\mathbf{z},b}\left(\tilde{\mathbf{H}}_{\mathbf{z},b}, \tilde{\mathbf{H}}_{\mathbf{r}-\mathbf{z},b}\right) = c_{\mathbf{z},b}\left(\tilde{\mathbf{H}}_{\mathbf{z},b}\right) \log_2\left(1 + \frac{P_{\mathbf{z},b}\left(\tilde{\mathbf{H}}_{\mathbf{z},b}\right)}{F_{\mathbf{z},b}\left(\tilde{\mathbf{H}}_{\mathbf{z},b}, \tilde{\mathbf{H}}_{\mathbf{r}-\mathbf{z},b}\right) + N_0}\right). \tag{25}$$

The proposed MAMA metric is defined as a scalar function designed to mirror the Hartley-Shannon spectral efficiency. It is comprised of three components, each designed to address distinct channel properties. In the following, we present each component along with its physical significance.

1) AVERAGE CHANNEL GAIN

The first component of the proposed metric in eq. (25) is the average channel gain $P_{\mathbf{z},b}$ provided by cell b along segment $\mathbf{z}$, and it is computed as follows,

$$P_{\mathbf{z},b}\left(\tilde{\mathbf{H}}_{\mathbf{z},b}\right) = \frac{1}{N_z}\sum_{z}^{N_z} \frac{1}{M}\sum_{m}^{M}\left|\tilde{h}_{m,z,b}\right|^2, \tag{26}$$

This term offers insight into the average channel gain that a UAV can expect from a cell in a given segment, similarly to traditional RSRP-based association.

2) CHANNEL DIVERSITY ASSESSMENT

The second element of our metric is the inverse of the condition number of matrix $\tilde{\mathbf{H}}_{\mathbf{z},b}$ [52], referred to as $c_{\mathbf{z},b}$, and defined as follows,

$$c_{\mathbf{z},b}\left(\tilde{\mathbf{H}}_{\mathbf{z},b}\right) = \frac{\lambda_{\mathbf{z},b}^{(M-1)}\left(\tilde{\mathbf{H}}_{\mathbf{z},b}\right)}{\lambda_{\mathbf{z},b}^{(0)}\left(\tilde{\mathbf{H}}_{\mathbf{z},b}\right)}, \tag{27}$$

This component offers insights into the expected spatial multiplexing capabilities of cell b with respect to the considered segment $\mathbf{z}$.

To compute this scalar component for segment $\mathbf{z}$, we consider the expected complex channel matrix $\tilde{\mathbf{H}}_{\mathbf{z},b}$ and we compute its set of singular values using single value decomposition (SVD). Those are then organized into vector $\boldsymbol{\lambda}_{\mathbf{z},b}$ in decreasing order, as follows:

$$\boldsymbol{\lambda}_{\mathbf{z},b}\left(\tilde{\mathbf{H}}_{\mathbf{z},b}\right) = \left[\lambda_{\mathbf{z},b}^{(0)}, \lambda_{\mathbf{z},b}^{(1)}, \ldots, \lambda_{\mathbf{z},b}^{(M-1)}\right]^T. \tag{28}$$

It should be noted that, maintaining a minimum segment length (number of points within the segment greater than the number of antennas ensures that the cardinality of the singular values vector is equal to M. We then derive $c_{\mathbf{z},b}$ as the ratio between the lowest and highest singular value of vector $\boldsymbol{\lambda}_{\mathbf{z},b}$, as defined in eq. (27). This ratio serves as a crucial component of our metric, offering insights into the spread of singular values and the variation of AoAs/AoDs across the segment concerning each cell, thereby assessing the diversity of the complex channels to enable higher and fairer UE data rates. Note that this metric, defined as the inverse of the condition number, decreases with the increasing singular values spread and, therefore, increases with AoAs/AoDs diversity. Moreover, it bounds its values in the range [0, 1], preventing undefined operations when the lowest singular value is zero.

3) INTER-CELL INTERFERENCE ASSESSMENT

The last component is the squared Frobenius norm, $F_{\mathbf{z},b}$, of the cross-correlation matrix between the two matrices $\tilde{\mathbf{H}}_{\mathbf{z},b}, \tilde{\mathbf{H}}_{\mathbf{r}-\mathbf{z},b}$, and it is defined as follows,

$$F_{\mathbf{z},b}\left(\tilde{\mathbf{H}}_{\mathbf{z},b},\ \tilde{\mathbf{H}}_{\mathbf{r}-\mathbf{z},b}\right) = \|\tilde{\mathbf{H}}_{\mathbf{r}-\mathbf{z},b}\tilde{\mathbf{H}}_{\mathbf{z},b}^H\|_F^2 = \sum_{i}^{N_r-N_z}\sum_{z}^{N_z}\left|\sum_{m}^{M}\tilde{h}_{m,i,b}\,\tilde{h}^*_{m,z,b}\right|^2. \tag{29}$$

This component allows us to gain insight into the interference generated from cell b, which is using different precoders to serve UAVs in segment $\mathbf{z}$, to UAVs located over the remaining part of the AH. Then, considering UAVs in each discrete point, the expected inter-cell interference introduced on the remaining segments can be computed as:[2]

$$\tilde{\mathbf{i}}_{\mathbf{r}-\mathbf{z},b}^{\mathrm{inter}} = \left|\tilde{\mathbf{H}}_{\mathbf{r}-\mathbf{z},b}\,\mathbf{W}_{\mathbf{r}-\mathbf{z},b}^{\mathrm{dl}}\right|^2 \mathbf{e}, \tag{30}$$

where we recall that $\mathbf{e}$ is defined as a vector of all ones. As described in Section II-C, during the UE's data precoding phase, the network depends on the selection of the codeword that maximizes UEs' received power. This can be interpreted as the choice of precoders that better approximate the Hermitian of the channels, i.e.,

$$\mathbf{W}_{\mathbf{r}-\mathbf{z},b}^{\mathrm{dl}} = \arg\min_{\mathbf{W}_{\mathbf{r}-\mathbf{z},b}^{\mathrm{dl}}}\left\{\left\|\tilde{\mathbf{H}}_{\mathbf{z},b}\,\tilde{\mathbf{H}}_{\mathbf{z},b}^H - \tilde{\mathbf{H}}_{\mathbf{z},b}\,\mathbf{W}_{\mathbf{r}-\mathbf{z},b}^{\mathrm{dl}}\right\|\right\} = \arg\min_{\mathbf{W}_{\mathbf{r}-\mathbf{z},b}^{\mathrm{dl}}}\left\{\left\|\tilde{\mathbf{H}}_{\mathbf{z},b}\left(\tilde{\mathbf{H}}_{\mathbf{z},b}^H - \mathbf{W}_{\mathbf{r}-\mathbf{z},b}^{\mathrm{dl}}\right)\right\|\right\}. \tag{31}$$

Thus, eq. (30) can be approximated as follows:

$$\tilde{\mathbf{i}}_{\mathbf{r}-\mathbf{z},b}^{\mathrm{inter}} \approx \tilde{\mathbf{i}}_{\mathbf{r}-\mathbf{z},b}^{\mathrm{inter}\prime} = \left|\tilde{\mathbf{H}}_{\mathbf{r}-\mathbf{z},b}\,\tilde{\mathbf{H}}_{\mathbf{z},b}^H\right|^2 \mathbf{e}. \tag{32}$$

Finally, we calculate $F_{\mathbf{z},b}$ as the squared Frobenius norm of the obtained cross-correlation channel matrix, as described in eq (29).

[2]Note that, in eqs.(30) and (32), the term $|\cdot|^2$ represents the element-wise squared absolute operation.

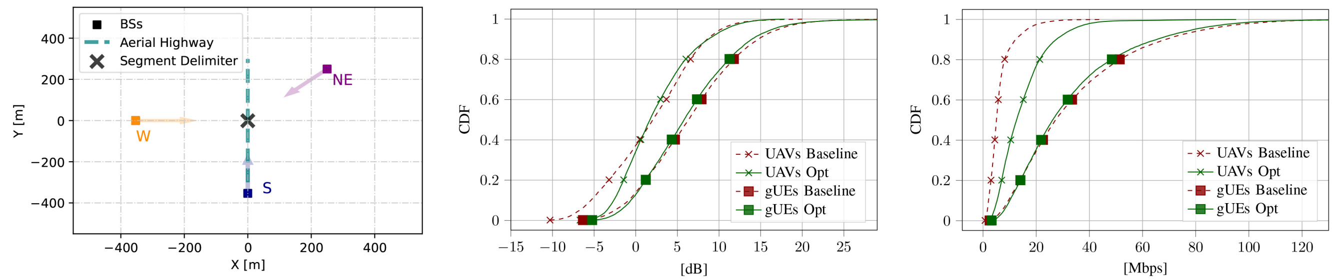

(a) Simplified 2D Layout (b) SINR Distribution (c) Achievable Data Rate Distribution

FIGURE 3. Comparison of UAVs SINR distribution (Figure 3(a)) and achievable data rate distribution (Figure 3(b)) in the simplified scenario (Figure 3(c)).

This last component offers insights into the potential introduced interference, particularly crucial in typical LoS scenarios where lower channel gains from neighbouring cells do not mitigate inter-cell interference.

B. AERIAL SEGMENT SERVING CELL SELECTION

Mirroring the Hartley-Shannon spectral efficiency, the three aforementioned components $F_{\mathbf{z},b}(\cdot,\cdot)$, $c_{\mathbf{z},b}(\cdot)$ and $P_{\mathbf{z},b}(\cdot)$, are melted together to compute the MAMA metric $\chi_{\mathbf{z},b}$, as defined in eq. (25). Then, leveraging MAMA, the designed serving cell $\hat{b}_{\mathbf{z}}$ for each segment $\mathbf{z}$ is computed as follows,

$$\hat{b}_{\mathbf{z}} = \arg\max_{b\in\mathcal{B}} \left\{ \chi_{\mathbf{z},b}\left(\tilde{\mathbf{H}}_{\mathbf{z},b}, \tilde{\mathbf{H}}_{\mathbf{r}-\mathbf{z},b}\right) \right\}. \tag{33}$$

This scalar metric exploits the prior information of the AH to blend together important and different network physical aspects, such as the expected average gain that UAVs will perceive while flying along it, the cell capability of multiplexing different UAVs on the same PRBs and the introduced interference to other segments. Therefore, this metric allows us to select the serving cell that offers the most effective trade-off among them.

C. ILLUSTRATIVE EXAMPLE

To illustrate the advantages of the proposed metric in selecting the serving cell for UAVs within AHs, we present results in a simplified scenario based on the system model described in Section II. More complex scenarios will be studied in Section VI. Consider the scenario depicted in Figure 3(c), where three single-sector base stations are positioned at the Southern (S), Western (W), and Northeastern (NE) edges, at a height of 25 m. An AH passes from south to north over the centre of the scenario. For illustration purposes, we divide the AH into two segments: Northern and Southern. In this configuration, each sector broadcasts 8 SSB beams covering its designated area. All beams are tilted at 105° and span the azimuth plane. In the reference setup, referred to as "Baseline", when UAVs traverse the AH and measure the received power from different cells, they tend to associate with the S cell due to higher measured RSRP. However, UAVs appear almost collinear (i.e., one behind the other) from S cell viewpoint, and this cell cannot efficiently exploit its spatial multiplexing capabilities. Furthermore, this association introduces high interference on the AH to UAVs not connected to the S cell. In contrast, when selecting the serving cell according to the proposed MAMA metric, we find that UAVs on the Southern segment are served by the E cell, while UAVs in the Northern segment are served by the NE one. We refer to this scenario as "Opt".

TABLE 2. Summary of results for the scenario in Figure 3.

	KPI			
	$\text{SINR}_{5\%-\text{tile}}$ dB	$\text{SINR}_{\text{mean}}$ dB	$\text{Rate}_{5\%-\text{tile}}$ Mbps	$\text{Rate}_{\text{mean}}$ Mbps
Baseline	-6.73	1.88	1.60	6
Opt	-3.47	2.40	4	15
Gain	3.26	0.52	250%	250%

Figure 3 shows results in terms of SINR and achievable data rate distributions. It should be noted that a gain of 3.26 dB and a percentage gain of 250% are achieved for the 5%-tile of UAVs' SINR and achievable data rate, respectively. In Table 2, results are summarized in terms of 5%-tile and mean value. This scenario demonstrates the clear benefits of the proposed metric in optimizing cell association for UAVs within AHs, leading to improved performance.

V. PROPOSED SOLUTION

In this section, we introduce a heuristic approach designed to efficiently tackle Problem (1) and finding the optimal SSB planning solution. This approach divides the overall problem into two sub-problems: i) AH split and segment-to-cell association and ii) SSBs beam and transmit power selection.

The initial sub-problem focuses on segmenting the AH and identifying the most suitable serving cell for each segment. This process aims to maximize our proposed metric MAMA. Building on this, the resolution of the first sub-problem guides the approach for the second sub-problem, which narrows down the search to identify the most efficient combination of SSB beams to be deployed at each cell to ensure an optimal association between UAVs and cells, in alignment with the findings from the first sub-problem.

A. AERIAL HIGHWAY SPLIT AND SEGMENT-TO-CELL ASSOCIATION SUB-PROBLEM

By leveraging a priori planning information of the AH, and the proposed metric in Section IV, in the following, we formulate the first sub-problem as follows:

Problem 2: Aerial Highway Split and Segment-To-Cell Association

$$\max_{\mathcal{Z}_{\text{AH}}^{\text{split}},\hat{\mathbf{b}}_{\mathbf{z}}^{\text{split}}} \sum_{\mathbf{z}\in\mathcal{Z}_{\text{AH}}^{\text{split}}} \chi_{\mathbf{z},b_z}\left(\tilde{\mathbf{H}}_{\mathbf{z},b_z},\tilde{\mathbf{H}}_{\mathbf{r}-\mathbf{z},b_z}\right)$$

$$\begin{aligned} \text{s.t } & \cup_{\mathbf{z}\in\mathcal{Z}_{\text{AH}}^{\text{split}}} = \mathcal{Z}_{\text{AH}}^{\text{split}} \quad (C2.1) \\ & \mathbf{z}_i \cap \mathbf{z}_j = \emptyset,\ \forall \mathbf{z}_i,\mathbf{z}_j \in \mathcal{Z}_{\text{AH}}^{\text{split}} \quad (C2.2) \\ & \cup_i \mathbf{z}_i = \mathbf{r}_{\text{AH}} \quad (C2.3) \\ & b_{\mathbf{z}_i} \neq b_{\mathbf{z}_j},\ \forall b_{\mathbf{z}_i}, b_{\mathbf{z}_j} \in \hat{\mathbf{b}}_{\mathbf{z}}^{\text{split}} \quad (C2.4) \\ & \text{Card}\left\{\mathcal{Z}_{\text{AH}}^{\text{split}}\right\} = \text{Card}\left\{\hat{\mathbf{b}}_{\mathbf{z}}^{\text{split}}\right\}. \quad (C2.5) \end{aligned} \quad \text{(P2)}$$

Our goal is to identify the set of segments $\mathcal{Z}_{\text{AH}}^{\text{split}}$ and the corresponding set of serving cells $\hat{\mathbf{b}}_{\mathbf{z}}^{\text{split}}$ that maximizes the sum of our proposed MAMA metric for each segment. In the problem formulation outlined, solutions must satisfy the following constraints:

- C2.1, guaranteeing the representation of the set $\mathcal{Z}_{\text{AH}}$ through the union of all obtained segment.
- C2.2, mandating mutual disjoint condition for each pair of segments.
- C2.3, ensuring the representation of the all overall AH $\mathbf{r}_{\text{AH}}$ by consecutive concatenation of segments.
- C2.4, requiring a unique serving cell for each segment.
- C2.5, imposing the number of total segments equals the number of serving cells.

Collectively, constraints $C2.2$, $C2.4$, and $C2.5$ define a bijective relationship between the set of segments and the set of serving cells, guaranteeing a unique pairing between each segment and its corresponding serving cell.

B. AERIAL HIGHWAY SPLIT ALGORITHM

In the following sections, we introduce an algorithm based on PSO [53], [54], [55], aimed at addressing Problem (P2). This algorithm is structured into two main components: i) an outer loop, as detailed in Algorithm 1, which aims to determine the optimal number of segments; ii) an inner loop, outlined in Algorithm 2 and referred to as Particle Aerial Highway Swarm Segmentation (PAHSS), specifically designed to ascertain the most efficient dimension of each segment, while establishing for each segment the optimal serving cell via MAMA metric.

1) OUTER LOOP SPLIT ALGORITHM

Algorithm 1 systematically iterates over the number of segments n_s, starting from a minimum value $N_{\text{seg}}^{\min}$ and incrementing up to a maximum threshold $N_{\text{seg}}^{\max}$. During each iteration, the current number of segments and $\mathbf{r}_{\text{AH}}$ serve as inputs to the PAHSS algorithm.

The iteration process continues until one of two conditions is met: either the process exhausts the range of segment numbers, reaching $N_{\text{seg}}^{\max}$, or it encounters a specific intermediate stopping condition. This condition evaluates whether any pair of neighbouring segments are assigned to the same serving cell; if they are, these segments can be represented by a unique one, thereby falling under the previous case, i.e., n_s-1. Thus, if such a scenario is detected, the algorithm halts, adopting the configuration from the preceding iteration as its final output.

Algorithm 1: Outer Loop Split Algorithm

Data: $\mathbf{r} \leftarrow \mathbf{r}_{\text{AH}}$
Result: $\mathcal{Z}_{\text{AH}}^{\text{split}}, \hat{\mathbf{b}}_{\mathbf{z}}^{\text{split}}$

$\mathcal{Z}_{\text{AH}}^{(opt)}, \hat{\mathbf{b}}_{\mathbf{z}}^{(\text{opt})} \leftarrow \text{PAHSS}(\mathbf{r}, 1)$;
for $n_s \in \left[N_{\text{seg}}^{\min}, N_{\text{seg}}^{\max}\right]$ **do**
  $\mathcal{Z}_{\text{AH}}^{(n_s)}, \hat{\mathbf{b}}_{\mathbf{z}}^{(\text{n}_\text{s})} \leftarrow \text{PAHSS}(\mathbf{r}, n_s)$;
  if $\exists \mathbf{z}_i, \mathbf{z}_j \in \mathcal{Z}_{\text{AH}}^{(n_s)} : b_{\mathbf{z}_i} = b_{\mathbf{z}_j}$ **then**
    $\mathcal{Z}_{\text{AH}}^{\text{split}} = \mathcal{Z}_{\text{AH}}^{(\text{opt})}$;
    $\hat{\mathbf{b}}_{\mathbf{z}}^{\text{split}} = \hat{\mathbf{b}}_{\mathbf{z}}^{(\text{opt})}$;
    Terminate;
  else
    $\mathcal{Z}_{\text{AH}}^{(\text{opt})} = \mathcal{Z}_{\text{AH}}^{(n_s)}$;
    $\hat{\mathbf{b}}_{\mathbf{z}}^{(\text{opt})} = \hat{\mathbf{b}}_{\mathbf{z}}^{(\text{n}_\text{s})}$;
  end
end
$\mathcal{Z}_{\text{AH}}^{\text{split}} = \mathcal{Z}_{\text{AH}}^{(n_s)}$;
$\hat{\mathbf{b}}_{\mathbf{z}}^{\text{split}} = \hat{\mathbf{b}}_{\mathbf{z}}^{(\text{n}_\text{s})}$;

2) PAHSS ALGORITHM

To find the optimal configuration for the indicated number of segments, we propose an evolutionary algorithm based on PSO [53], [54], [55], as it is a robust and fast method to solve non-convex non-linear, non-differentiable multidimensional problems.

In this work, each particle p represents an AH segmentation, represented by $\mathbf{x}^{(p)}$:

$$\mathbf{x}^{(p)} = \left[x_0^{(p)},\ldots,x_n^{(p)},\ldots,x_{n_s-2}^{(p)}\right]^T, \tag{34}$$

where n_s is the number of desired segments, and each element of this vector serves as a delimiter or boundary for the segments composing the aerial highway $\mathbf{r}_{\text{AH}}$, which we refer to as pivots.

Subsequently, for each AH segmentation p and its defined pivots $\mathbf{x}^{(p)}$, each segment $\mathbf{z}^{(p)} \in \mathcal{Z}_{\text{AH}}^{(n_s)}$ is delineated as the interval between two consecutive pivots. Specifically, this segmentation is represented as:

$$\mathbf{z}_0^{(p)} \doteq \left[r_0,\ x_0^{(p)}\right), \quad \mathbf{z}_{n_s}^{(p)} \doteq \left[x_{n_s-2}^{(p)},\ r_{-1}\right] \tag{35}$$

and

$$\forall n \in [0, n_s-2],\ \mathbf{z}_n^{(p)} \doteq \left[x_n^{(p)},\ x_{n+1}^{(p)}\right), \tag{36}$$

Algorithm 2: PAHSS Algorithm

Input: $\mathbf{r}$, n_s
Output: $\mathcal{Z}_{\mathrm{AH}}^{(n_s)}$, $\hat{\mathbf{b}}_{\mathbf{z}}^{(\mathrm{n_s})}$
$x_{\mathrm{LB}},\ x_{\mathrm{UB}} \leftarrow r_0,\ r_{-1}$;
$\mathcal{Z}_{\mathrm{AH}}^{(n_s)}, \hat{\mathbf{b}}_{\mathbf{z}}^{(\mathrm{n_s})} = \emptyset, \emptyset$;
$\mathbf{x}^{(p)} \leftarrow$ init_random_current_position$(\mathbf{r}, N_{\mathrm{swarm}}, n_s - 1)$;
$\mathbf{v}^{(p)} \leftarrow$ init_zeros_velocity$(N_{\mathrm{swarm}}, n_s - 1)$;
if $n_s = 1$ **then**
  $\mathcal{Z}_{\mathrm{AH}}^{(n_s)} \leftarrow \mathcal{Z}_{\mathrm{AH}}^{(n_s)} \cup \mathbf{r}$;
  $\hat{b}_{\mathbf{r}} \leftarrow \arg\max_{b\in\mathcal{B}}\left\{\chi_{\mathbf{r}}^{b}(\cdot)\right\}$;
  $\hat{\mathbf{b}}_{\mathbf{z}}^{(\mathrm{n_s})} \leftarrow \hat{\mathbf{b}}_{\mathbf{z}}^{(\mathrm{n_s})} \cup \hat{b}_{\mathbf{r}}$;
  Terminate;
end
for $i \in \left[0, N_{pso}^{\mathrm{Iter}} - 1\right]$ **do**
  for $p \in [0, N_{\mathrm{swarm}} - 1]$ **do**
    if $\mathrm{Obj}^{\mathrm{pso}}\left(\mathbf{x}_{\mathrm{best}}^{(p)}\right) < \mathrm{Obj}^{\mathrm{pso}}\left(\mathbf{x}^{(p)}\right)$ **then**
      $\mathbf{x}_{\mathrm{best}}^{(p)} \leftarrow \mathbf{x}^{(p)}$;
    end
    if $\mathrm{Obj}^{\mathrm{pso}}(\mathbf{x}_{\mathrm{best}}) < \mathrm{Obj}^{\mathrm{pso}}\left(\mathbf{x}_{\mathrm{best}}^{(p)}\right)$ **then**
      $\mathbf{x}_{\mathrm{best}} \leftarrow \mathbf{x}_{\mathrm{best}}[p]$;
    end
  end
  for $p \in [0, N_{\mathrm{swarm}} - 1]$ **do**
    $\mathbf{v}^{(p)} \leftarrow \omega\,\mathbf{v}^{(p)} + \phi_c c_1\left(\mathbf{x}_{\mathrm{best}}^{(p)} - \mathbf{x}^{(p)}\right) + \phi_s c_2\left(\mathbf{x}_{\mathrm{best}} - \mathbf{x}^{(p)}\right)$;
    $\mathbf{x}^{(p)} \leftarrow \mathbf{x}^{(p)} + \mathbf{v}^{(p)}$;
    if $\forall x_i^{(p)} \in \mathbf{x}^{(p)}, \exists x_i^{(p)} < x_{\mathrm{LB}}$ **then**
      $x_i^{(p)} \leftarrow x_{\mathrm{LB}}$;
    end
    if $\forall x_i^{(p)} \in \mathbf{x}^{(p)}, \exists x_i^{(p)} > x_{\mathrm{UB}}$ **then**
      $x_i^{(p)} \leftarrow x_{\mathrm{UB}}$;
    end
  end
end
$\mathbf{z}_0 \leftarrow \left[r_0,\ x_{\mathrm{best},0}\right)$;
$\mathbf{z}_{n_s} \leftarrow \left[x_{\mathrm{best},n_s-2},\ r_{-1}\right)$;
for $n \in [0, n_s - 2]$ **do**
  $\mathbf{z}_n \leftarrow \left[x_{\mathrm{best},n},\ x_{\mathrm{best},n+1}\right]$;
end
$\mathcal{Z}_{\mathrm{AH}}^{(n_s)} \leftarrow \mathcal{Z}_{\mathrm{AH}}^{(n_s)} \cup_{n}^{n_s} \mathbf{z}_n$;
for $\mathbf{z} \in \mathcal{Z}_{\mathrm{AH}}^{(n_s)}$ **do**
  $\hat{\mathbf{b}}_{\mathbf{z}}^{(\mathrm{n_s})} \leftarrow \hat{\mathbf{b}}_{\mathbf{z}}^{(\mathrm{n_s})} \cup \arg\max_{b\in\mathcal{B}}\left\{\chi_{\mathbf{z}}^{b}(\cdot)\right\}$;
end

where the first and last segments' bounds are defined by the limits of the AH, represented in eq. (35). Notably, r_0 and r_{-1} denote the initial and final elements of the AH, respectively.

Based on the derived segmentation, for each segment $\mathbf{z}$, the expected complex matrices $\tilde{\mathbf{H}}_{\mathbf{z},b}$ and $\tilde{\mathbf{H}}_{\mathbf{r}-\mathbf{z},b}$, representing channels between each segment $\mathbf{z}$ and each cell b are calculated, and the objective function to maximize for our PSO algorithm is then computed as the summation of the maximum MAMA metric for every segment with respect to each cell, as follows,

$$\mathrm{Obj}^{\mathrm{pso}}(\mathbf{x}_p) \doteq \sum_{\mathbf{z}\in\mathcal{Z}_{\mathrm{AH}}^{(p)}} \max_{b\in\mathcal{B}}\left(\chi_{\mathbf{z},b}\left(\tilde{\mathbf{H}}_{\mathbf{z},b}, \tilde{\mathbf{H}}_{\mathbf{r}-\mathbf{z},b}\right)\right). \quad (37)$$

The position $\mathbf{x}^{(p)}$ of each particle p, iteration after iteration, is adjusted according to its velocity $\mathbf{v}^{(p)}$, defined as follows,

$$\mathbf{v}^{(p)} \leftarrow \omega\,\mathbf{v}^{(p)} + \phi_c\, c_1\left(\mathbf{x}_{\mathrm{best}}^{(p)} - \mathbf{x}^{(p)}\right) + \phi_s\, c_2\left(\mathbf{x}_{\mathrm{best}} - \mathbf{x}^{(p)}\right) \quad (38)$$

$$\mathbf{x}^{(p)} \leftarrow \mathbf{x}^{(p)} + \mathbf{v}^{(p)} \quad (39)$$

Specifically, in velocity definition, ω represents the inertia weight, the term ϕ_c is the cognitive coefficient, and ϕ_s is the social coefficient. The constants c_1 and c_2 are random numbers within the range [0, 1], introducing stochasticity into the velocity update. The cognitive component ϕ_c accounts for the particle's personal best position it has encountered $\mathbf{x}_{\mathrm{best}}^{(p)}$, promoting the exploration of promising regions based on individual experience. Conversely, the social component ϕ_s considers the global best position found by any particle in the swarm $\mathbf{x}_{\mathrm{best}}$, encouraging convergence towards optimal solutions discovered collectively. During each iteration i, the algorithm updates the personal best position $\mathbf{x}_{\mathrm{best}}^{(p)}$ for each particle p if a better position is found. Similarly, the global best position $\mathbf{x}_{\mathrm{best}}$ is updated if a new optimal solution is discovered by the swarm. The algorithm proceeds until it either reaches a predefined number of iterations $N_{\mathrm{pso}}^{\mathrm{Iter}}$ or an early stopping criterion is met, based on the convergence of particles towards the global best position $\mathbf{x}_{\mathrm{best}}$. Upon termination of the iterative process, the MAMA metric is adopted to compute the optimal serving cell for each obtained segment (see eq. (33)), thereby defining the set $\hat{\mathbf{b}}_{\mathbf{z}}$. It should be noted that this operation retrieves the set of serving cells that maximized objective function (37). Detailed steps of the algorithm, are outlined in Algorithm 2.

C. SSB BEAMS AND TRANSMIT POWER SELECTION SUB-PROBLEM

Building upon the split and serving cell resulting from Algorithm 1, we formulate a problem to select codewords from a fixed codebook $\mathbf{W}^{\mathrm{ssb}}$ and their transmit power for each identified serving cell. The goal is to determine the optimal value for $\mathbf{X}$ and $\mathbf{P}$, respectively representing the SSBs codeword selection matrix and their transmit power levels, for maximizing the minimum expected SSB SINR over the AH across multiple channel realizations, therefore providing a reliable solution that is robust to different environmental conditions and ensures optimal network coverage from the set of serving cells $\hat{\mathbf{b}}_{\mathbf{z}}^{\mathrm{split}}$ determined by Algorithm 1. The problem is formulated as follows:

Problem 3: SSB Beams and Transmit Power Selection

$$\max_{\mathbf{X},\mathbf{P}}\ \min\left(\left\{\mathbb{E}_{\tau,\mathbf{h}^{\mathrm{dl}}}\left\{\gamma_r^{\mathrm{ssb}}(\mathbf{X}, \mathbf{P})\right\} \mid \forall r \in \mathbf{r}_{\mathrm{AH}}\right\}\right)$$

$$\text{s.t. } \hat{b}_z = \hat{b}_{\mathbf{z}}^{\text{split}}, \forall \mathbf{z} \in \mathcal{Z}_{\text{AH}}^{\text{split}}, \ \forall z \in \mathbf{z} \quad (C3.1)$$
$$\sum_{s}^{N_{CB}} x_{s,b} = N_{\text{ssb}}, \forall b \in \mathcal{B}, \quad (C3.2)$$
$$\frac{1}{2}\sum_{s}^{N_{CB}}\left(1 - x_{s,b}\, x_{s,b}^{\text{bl}}\right) \leq 1, \forall b \in \hat{\mathbf{b}}_{\mathbf{z}}^{\text{split}} \quad (C3.3)$$
$$0 \leq p_{s,b}^{\text{ssb}} \leq p_{\max}^{\text{ssb}}, \forall p_{s,b}^{\text{ssb}} \in \mathbf{P} \,|\, b \in \hat{\mathbf{b}}_{\mathbf{z}}^{\text{split}} \quad (C3.4)$$
$$x_{s,b} = x_{s,b}^{\text{bl}}, \forall s, \forall b \in \mathcal{B} \setminus \hat{\mathbf{b}}_{\mathbf{z}}^{\text{split}} \quad (C3.5)$$
$$p_{s,b}^{\text{ssb}} = p_{\max}^{\text{ssb}}, \quad \forall p_{s,b}^{\text{ssb}} \in \mathbf{P} \,|\, b \notin \hat{\mathbf{b}}_{\mathbf{z}}^{\text{split}} \quad (C3.6)$$
$$\mathbf{X} \in \{0, 1\}^{N_{CB} \times N_{BS}} \quad (C3.7)$$
$$\mathbf{P} \in \mathbb{R}^{N_{CB} \times N_{BS}} \quad (C3.8). \ \text{(P3)}$$

Feasible solution to Problem (3) must satisfy the following constraints:

- C3.1, imposing the serving cell for each point of segment $\mathbf{z}$, as specified by Algorithm 1 outcome.
- C3.2, specifying, for each cell b, the maximum number of deployed SSB beams to N_{ssb}.
- C3.3, restricting the permissible modifications of each cell within the set $\hat{\mathbf{b}}_{\mathbf{z}}^{\text{split}}$ to 1.
- C3.4, limiting the SSB beams transmitting power for cell withing the set $\hat{\mathbf{b}}_{\mathbf{z}}^{\text{split}}$.
- C3.5 and C3.6, mandating no modification with respect to baseline configuration $\mathbf{X}^{\text{bl}}$, $\mathbf{P}^{\text{bl}}$, for cells not in the set $\hat{\mathbf{b}}_{\mathbf{z}}^{\text{split}}$; thereby preserving the network's baseline performance and stability.
- C3.7 and C3.8, defining $\mathbf{X}$ and $\mathbf{Y}$ matrices space.

Relative to Problem (1), the complexity of Problem (3) is significantly reduced. This simplification arises from the predetermined set of serving cells $\hat{\mathbf{b}}_{\mathbf{z}}$, which narrows the search space to these cells exclusively. Furthermore, by limiting the number of beam changes to a maximum of one (as specified in $C3.3$), the spectrum of potential configurations is significantly condensed.

In the rest of the section, we first define a practical antenna panel structure designed to generate codebook entries via 2D-DFT and then we introduce an algorithm to solve Problem (3) efficiently.

D. PANEL STRUCTURE AND SSB CODEBOOK

Mirroring real-world scenarios, our model entails connecting each antenna element of the mMIMO planar array to a transceiver. To accommodate beams with varied beamwidths and beamforming gains, we adopt a switching pattern that begins deactivating antenna columns from the rightmost to the leftmost column.

In the i-th configuration, $M_h^{(i)}$ antenna columns are active, with i denoting the number of deactivated antenna columns. Consequently, the total count of active antennas $M^{(i)}$ is determined by $M_h^{(i)} \times M_v$. Utilizing this configuration, the 2D-DFT codebook $\mathbf{W}^{(i)} \in \mathbb{C}^{M^{(i)} \times M^{(i)}}$ is meticulously computed to embody the beamforming characteristics of the active antenna framework. The final codebook $\mathbf{W}^{\text{ssb}} \in \mathbb{C}^{M \times N_{CB}}$ is defined as follows:

$$\mathbf{W}^{\text{ssb}} = \left[\bar{\mathbf{W}}^{(0)} \,\middle|\, \bar{\mathbf{W}}^{(1)} \,\middle|\, \ldots \,\middle|\, \bar{\mathbf{W}}^{(M_h-1)}\right], \tag{40}$$

with

$$\bar{\mathbf{W}}^{(i)} = \mathbf{F}_{M,M^{(i)}}\, \mathbf{W}^{(i)}, \tag{41}$$

where $\mathbf{F}_{M,M^{(i)}}$ facilitates the mapping of codewords from active to full antenna configurations by inserting zeros for deactivated antennas. Recall that M is the total number of antennas in the antenna panel, and N_{CB} is the total number of codewords. Specifically, $\mathbf{F}_{M,M^{(i)}}$ is defined as follows,

$$\mathbf{F}_{M,M^{(i)}} \in \{0, 1\}^{M \times M^{(i)}}, \tag{42}$$

$$\mathbf{F}_{M,M^{(i)}} = \left.\overbrace{\begin{bmatrix} \mathbf{I}_{M_h,M_h^{(i)}} & \boldsymbol{\emptyset}_{M_h,M_h^{(i)}} & \boldsymbol{\emptyset}_{M_h,M_h^{(i)}} \\ \boldsymbol{\emptyset}_{M_h,M_h^{(i)}} & \mathbf{I}_{M_h,M_h^{(i)}} & \boldsymbol{\emptyset}_{M_h,M_h^{(i)}} \\ \boldsymbol{\emptyset}_{M_h,M_h^{(i)}} & \boldsymbol{\emptyset}_{M_h,M_h^{(i)}} & \mathbf{I}_{M_h,M_h^{(i)}} \end{bmatrix}}^{M_v}\right\} M_v. \tag{43}$$

Matrix $\mathbf{F}_{M,M^{(i)}}$ is composed, both vertically and horizontally, of M_v sub-matrix blocks. $\mathbf{I}_{M_h,M_h^{(i)}}$ denotes an identity matrix reflecting the active antennas, while $\boldsymbol{\emptyset}_{M_h,M_h^{(i)}}$ represents a zeros matrix corresponding to the deactivated ones.

E. BEAM AND POWER SELECTION GENETIC ALGORITHM

In this section, we present an evolutionary algorithm tailored to address Problem (3), employing a GA framework recognized for its efficacy in solving non-convex mixed-integer optimization problems [55], [56], [57]. To enhance the standard GA procedure, we incorporate an elite selection mechanism [58], henceforth referred to as eGA.

Echoing the approach used in PSO, our eGA initiates its search with a randomly generated population. This population iteratively evolves, guided by a fitness function, towards an optimal solution across successive generations. Within this framework, each individual, denoted as q, symbolizes a feasible solution to the posed problem. The representation of each individual is a multi-dimensional vector, elaborated as follows:

$$\begin{aligned} \mathbf{y}^{(q)} &= \left[\mathbf{s}_{\hat{\mathbf{b}}_{\mathbf{z}}}^{(q)} \,\middle|\, \mathbf{p}_{\hat{\mathbf{b}}_{\mathbf{z}}}^{\text{ssb}\,(q)}\right] \\ &= \left[s_{b_0}^{(q)}, \ldots, s_{b_{n_s}}^{(q)} \,\middle|\, p_{b_0}^{\text{ssb}\,(q)}, \ldots, p_{b_{n_s}}^{\text{ssb}\,(q)}\right], \end{aligned} \tag{44}$$

with

$$\forall s_{b_{\mathbf{z}}}^{(q)} \in \mathbf{s}_{\hat{\mathbf{b}}_{\mathbf{z}}}^{(q)}, \ s_{b_{\mathbf{z}}}^{(q)} \in [0, N_{CB}], \tag{45}$$

$$\forall p_{b_{\mathbf{z}}}^{\text{ssb}\,(q)} \in \mathbf{p}_{\hat{\mathbf{b}}_{\mathbf{z}}}^{\text{ssb}\,(q)}, \ 0 \leq p_{b_{\mathbf{z}}}^{\text{ssb}\,(q)} \leq p_{\max}^{\text{ssb}}, \tag{46}$$

where $s_{b_{\mathbf{z}}}$ indicates the index of the selected beam from a codebook containing N_{CB} entries for cell $b_{\mathbf{z}}$ within subset $\hat{\mathbf{b}}_{\mathbf{z}}^{\text{split}}$, and $p_{b_{\mathbf{z}}}^{\text{ssb}}$ represents its transmitting power. Matrices $\mathbf{X}^{(q)}$ and $\mathbf{P}^{(q)}$ are subsequently determined based on $\mathbf{y}^{(q)}$.

The evolutionary progress across generations is governed by a fitness/objective function as specified in eq. (47), as

Algorithm 3: Elite Genetic Algorithm Beam and Power Selection

Data: $\mathcal{Z}_{\mathrm{AH}}^{\mathrm{split}}$, $\hat{\mathbf{b}}_{\mathbf{z}}^{\mathrm{split}}$
Result: $\mathbf{y}_{\mathrm{best}}$

$\mathbf{y}^{(p)} \leftarrow$ init_random_population$\left(N_{\mathrm{pop}}, N_{CB}, p_{\max}^{\mathrm{ssb}}\right)$;
$\mathbf{f} \leftarrow$ init_zeros$\left(N_{\mathrm{pop}}\right)$;
for $i \in \left[0, N_{eGA}^{\mathrm{Iter}} - 1\right]$ **do**
  for $q \in \left[0, N_{\mathrm{pop}} - 1\right]$ **do**
    $\mathbf{f}[q] \leftarrow \mathrm{Obj}^{\mathrm{eGA}}\left(\mathbf{y}^{(q)}\right)$;
  end
  sort_population($\mathbf{f}$);
  $\mathbf{y}_{\mathrm{best}} \leftarrow \mathbf{y}^{(0)}$;
  $\mathbf{par}_e \leftarrow \left[\mathbf{y}^{(0)}, \mathbf{y}^{(N_e)}\right]$;
  $\mathbf{par}_q \leftarrow \left[\mathbf{y}^{(0)}, \mathbf{y}^{(N_p)}\right]$;
  for $q \in N_{\mathrm{cross}}$ **do**
    $\mathbf{y}^{(i)}, \mathbf{y}^{(j)} \leftarrow$ randomUniform_selPair($\mathbf{par}_q$);
    for $k \in 0, [2n_s - 1]$ **do**
      if random() $\leq P_{\mathrm{cross}}$ **then**
        $\mathbf{y}^{(i)}[k], \mathbf{y}^{(j)}[k] \leftarrow \mathbf{y}^{(j)}[k], \mathbf{y}^{(i)}[k]$;
      end
    end
  end
  for $q \in 0, \left[N_{\mathrm{pop}} - 1\right]$ **do**
    for $k \in [0, n_s - 1]$ **do**
      if random() $\leq P_{\mathrm{mut}}$ **then**
        $\mathbf{y}^{(q)}[k] \leftarrow$ randInt$(0, N_{CB} - 1)$;
      end
    end
    for $k \in [n_s, 2n_s - 1]$ **do**
      if random() $\leq P_{\mathrm{mut}}$ **then**
        $\mathbf{y}^{(q)}[k] \leftarrow$ rand$\left(0, p_{\max}^{\mathrm{ssb}}\right)$;
      end
    end
  end
  $e \leftarrow 0$;
  for $q \in \left[N_{\mathrm{pop}} - N_e, N_{\mathrm{pop}} - 1\right]$ **do**
    $\mathbf{y}^{(q)} \leftarrow \mathbf{par}_e[e]$;
    $e \leftarrow e + 1$;
  end
end

shown at the bottom of the page, where for each point z in a segment the expected SINR is computed, with γ_z^{ssb} calculated in accordance with eq. (13). By considering the expected SINR across multiple shadowing and fast fading realizations, it is possible to account for different channel conditions, therefore providing robust solutions that can adapt to varying environmental conditions. Moreover, for each point, the assigned serving cell is determined as per the outcomes of the segmentation and selection process detailed in Algorithm 1, with the designated serving SSB beam and its transmit power being set in accordance with $\mathbf{y}^{(q)}$. To accommodate this network variation, $\mathbf{X}$ and $\mathbf{P}$ are updated, accordingly to $\mathbf{y}^{(q)}$, to reflect these selections and their implications on the network configuration. In this work we consider all the modified SSB beams at cells $\hat{\mathbf{b}}_{\mathbf{z}}^{\mathrm{split}}$ associated with the same i^{ssb} sweep index.

In the eGA, three key operations permit the transmission of information from one generation of the population to the next. These operations are crucial for the evolutionary process: *i)* Selection: individuals/solutions of the population are ranked by their objective function, with the top N_p of them chosen as parents for the next generation. The highest-ranking individual is noted as the generation's optimal solution. *ii)* Crossover: with a chance P_{cross}, elements of $\mathbf{y}^{(q)}$ for a random pair of parents are exchanged, thereby creating offspring that blend traits from both. This operation is crucial for diversity and exploration of the searching space. *iii)* Mutation: elements of the new created individuals $\mathbf{y}^{(q)}$ (i.e., offsprings) are randomly changed with probability P_{mut}. This step is crucial for diversity and overcoming saddle points. In addition, the algorithm incorporates an "elastic parent selection" mechanism, for which the best N_e parents are directly passed to the next generation without undergoing crossover or mutation. This strategy helps to preserve excellent solutions from one generation to the next.

The algorithm iterates through these operations until it reaches a predefined number of generations, $N_{\mathrm{eGA}}^{\mathrm{Iter}}$, or the best solution does not change for a certain number of generations. In Algorithm 3, we present the details of the implementation of our eGA-based algorithm.

F. CONVERGENCE AND COMPLEXITY

In the following, we discuss convergence and the complexity of the proposed two-stage solution. Specifically, as previously discussed, we rely on two stages, in which the first, based on PSO, aims to optimally segment the AH, while the second, based on eGA, leverage the obtained segmentation and aim to find the optimal cell SSB beams and power configuration for desired cell coverage.

Figure 4 shows the evolution of the objective function for both PSO-based PAHSS algorithm and eGA-based beam and power selection algorithm. In Figure 4(a), we can observe that, as discussed in [59], the particles in the swarm tend to converge to the same position and objective function value, thereby converging to the optimal point. Specifically, assuming a swarm size of 50 particles, it converges in 40 iterations. Similarly, Figure 4 shows the objective function evolution of the fittest individual in the population for the eGA. Authors in [58], [60], [61] discussed the convergence of GA, showing how optimality is reached if the best

$$\mathrm{Obj}^{\mathrm{eGA}}\left(\mathbf{y}^{(q)}\right) := \min\left(\left\{\mathbb{E}_{\tau,\mathbf{h}^{\mathrm{dl}}}\left\{\gamma_z^{\mathrm{ssb}}\right\} \,\middle|\, \forall \mathbf{z} \in \mathcal{Z}_{AH}^{\mathrm{split}},\ \forall z \in \mathbf{z},\ \hat{b}_z = \hat{b}_{\mathbf{z}}^{\mathrm{split}},\ \hat{s}_z = s_{b_{\mathbf{z}}}^{(q)},\ p_{\hat{s}_z,\hat{b}_z}^{\mathrm{ssb}\,(q)} = p_{b_{\mathbf{z}}}^{\mathrm{ssb}},\ \mathbf{X} = \mathbf{X}^{(q)},\ \mathbf{P} = \mathbf{P}^{(q)}\right\}\right) \quad (47)$$

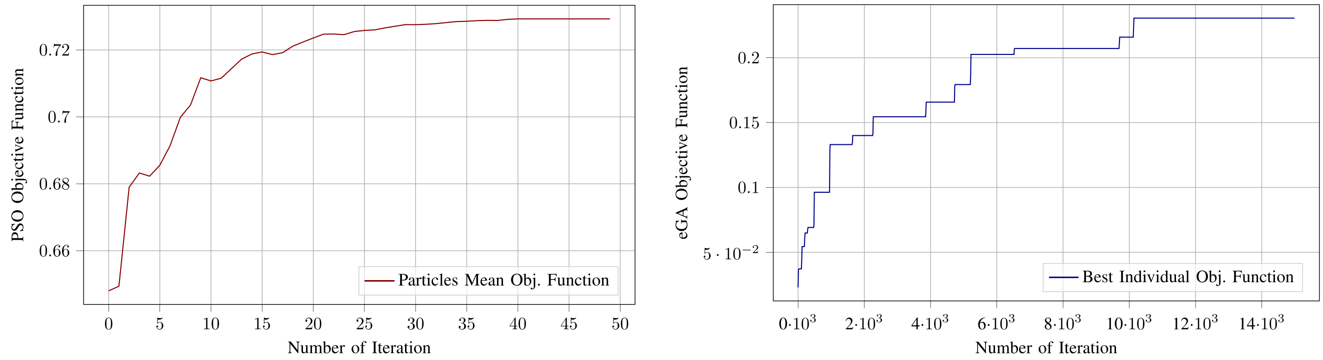

(a) PAHSS Objective Function Evolution

(b) eGA Objective Function Evolution

FIGURE 4. **Objective function evolution for PAHSS PSO-based algorithm (Figure 4(a)), and beam and power selection eGA-based algorithm (Figure 4(b)).**

TABLE 3. **Summary of algorithms hyperparameters.**

PAHSS (PSO)					
N_{pso}^{Iter}	N_{swarm}	ω	ϕ_c	ϕ_s	$(N_{\text{seg}}^{\min}, N_{\text{seg}}^{\max})$
50	100	0.75	0.75	90	(2, 12)
Beam and Power Selection (eGA)					
N_{eGA}^{Iter}	N_{pop}	P_{cross}	P_{mut}	N_p	N_e
15k	100	0.20	0.75	75	20

solution for each population is maintained and the mutation probability is greater than zero, therefore describing the eGA algorithm here implemented. Specifically, assuming a population size of 100 individuals, our eGA converge in 12k iteration.

Hyperparameters adopted for both Algorithms 2 and 3 are summarized in Table 3.

The total complexity of our proposed solution can be computed as the sum of the complexities of each stage, as they are connected in a cascading sequence. Therefore, the overall complexity C^{tot} is expressed as follows,

$$C^{\text{tot}} = C^{\text{split}} + C^{\text{eGA}} \tag{48}$$

where C^{split} and C^{eGA} are, respectively, the complexity of the AH split algorithm and the beam power eGA-based algorithm. Note that complexities depend on the number of segments of each iteration, therefore, in the rest of the section, we upper bound complexities by considering always the maximum admissible number.

Complexity C^{split} is driven by the number of iterations of the outer loop and the complexity of PAHSS algorithm C^{PAHSS}. So, complexity C^{split} scales as follows,

$$C^{\text{split}} = O\left(N_{\text{seg}}^{\max} C^{\text{PAHSS}\left(N_{\text{seg}}^{\max}\right)}\right), \tag{49}$$

where C^{PAHSS} follow the complexity of PSO algorithm [53], [59], and can be expressed as

$$C^{\text{PAHSS}} = O\left(N_{\text{pso}}^{\text{Iter}} N_{\text{swarm}} N_{\text{seg}}^{\max} N_r N_{\text{BS}} M^2\right), \tag{50}$$

where term $(N_r M^2)$ refer to SVD complexity, which drives the MAMA metric computation for all the N_{BS} cells, and term $N_{\text{seg}}^{\max}$ is the maximum number of admissible segments and refers to the maximum dimension of each particle within the swarm.

Considering the beam and power selection algorithm, its complexity C^{eGA} follows the one of eGA [55], [56], [57], and scales as,

$$C^{\text{eGA}} = O\left(N_{\text{eGA}}^{\text{Iter}} N_{\text{pop}}\left(\log_2\left(N_{\text{pop}}\right) + N_{\text{seg}}^{\max} + N_r\right)\right), \tag{51}$$

where term $\log_2(N_{\text{pop}})$ refer to crossover and mutation complexity, $N_{\text{seg}}^{\max}$ to each individual dimension and N_r to the objective function complexity computation.

Finally, combining the above equations, the complexity C^{tot} of the overall solution scales as:

$$C^{\text{tot}} = O\left(N_{\text{pso}}^{\text{Iter}} N_{\text{swarm}} N_{\text{seg}}^{\max^2} N_r N_{\text{BS}} M^2 + N_{\text{eGA}}^{\text{Iter}} N_{\text{pop}}\left(\log_2 N_{\text{pop}} + N_{\text{seg}}^{\max} + N_r\right)\right). \tag{52}$$

It should be noted that the overall complexity depends linearly on the number of points of the AH N_r and grows quadratically with the maximum number of admissible segments $N_{\text{seg}}^{\max}$, thus showing how the complexity scales with the dimension of the AH. Additionally, similar behaviour is observed for the number of cells in the network N_{BS} and the total number of antennas per sector M, which describes how the complexity evolves with the network deployment dimensions. Finally, the overall complexity scales linearly with almost all hyperparameters of PAHSS and the beam power eGA algorithm, with the exception of the population size in eGA, which suggests that it is preferable to increase the number of iterations instead of the population size for the optimal tuning of this algorithm.

VI. SIMULATION RESULTS

In this section, we examine UEs data SINR and data rate performance resulting from our proposed SSB beam planning solution. This analysis leverages the network and channel models detailed in Section II, focusing on UMa scenario with outdoor gUEs. This scenario is characterized by sites

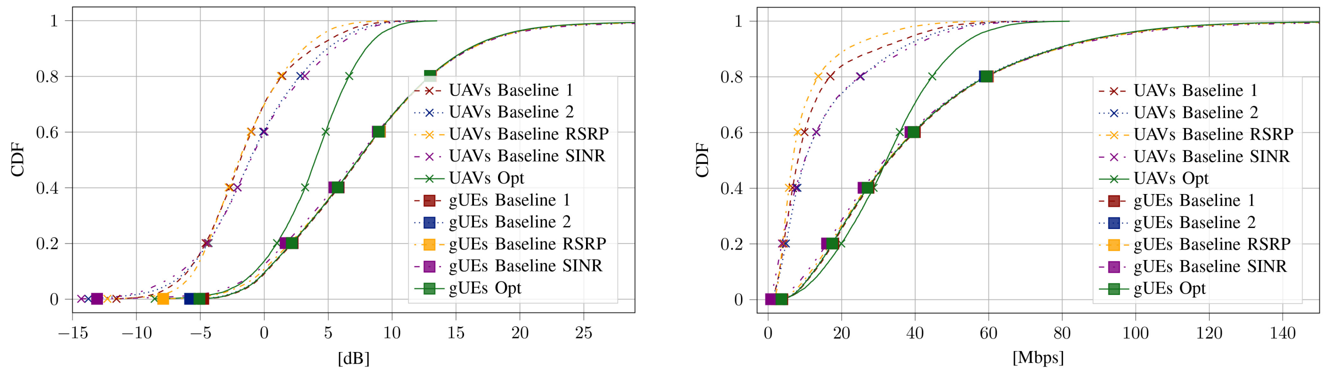

(a) SINR Distribution

(b) Achievable Data Rate Distribution

FIGURE 5. SINR and achievable data rate distribution considering 12 UAVs on a 1250 m herial highway positioned across cell edges at 100 m height.

spaced equally at a distance of $d_{\text{ISD}} = 500\,\text{m}$, with sectors at a height of $h_{\text{BS}} = 25\,\text{m}$. Each sector is equipped with an 8×4 UPA panel. The operating frequency is set at $f_c = 3.5\,\text{GHz}$, with 100 PRBs each of 180 kHz considered for the analysis.

It should be noted that in this work we do not aim to design real-time schedulers or transmission schemes that consider instantaneous network necessities and optimize the network accordingly. Instead, we focus on enhancing UAVs SINR and the achievable data rate by exclusively optimizing coverage through the planned SSB beams from the identified optimal serving cell set, thereby providing a stable solution that remains unchanged regardless of the instantaneous network dynamics. To the best of our knowledge, no existing works or algorithms specifically aim to optimize aerial coverage in 5G networks with the primary objective of enhancing the SINR and achievable data rates for UAVs. Therefore, to ensure a fair comparison of approaches, we will discuss and contrast our proposed solution with four different baseline configurations, which are designed based on conventional network coverage solutions. All of the considered baselines overall broadcast eight SSB beams over their azimuthal spread; however, they differ in configuration:

- Baseline 1 maintains a uniform tilt of 105° across all beams, as previously introduced in Section IV; this configuration aligns with conventional network setups designed primarily for gUEs, thus this configuration is used to setup matrix $\mathbf{X}^{\text{bl}}$.
- Baseline 2 adopts a hybrid approach by tilting the central beam to 75° and aligning the remaining beams as per Baseline 1.
- Baseline RSRP leverages the eGA proposed in Section V to find the optimal beams across all the network cells that maximize the SSB beam coverage RSRP footprint on the AH. Here, instead of using the previously discussed objective function with its constraints and searching only among the set of identified serving cells, this baseline considers all the cells within the network and aims to maximize the following objective function:

$$\text{Obj}^{\text{eGA}}_{\text{bl,rsrp}} := \min\Big(\Big\{\mathbb{E}_{\tau,\mathbf{h}^{\text{dl}}}\Big\{\text{rsrp}^{\text{ssb}}_{r}(\mathbf{X},\mathbf{P})\Big\} \mid \forall r \in \mathbf{r}_{\text{AH}}\Big\}\Big). \tag{53}$$

It should be noted that similar to Baseline 2, only the central beam of the cells is modified, with the remaining configured as per Baseline 1.
- Baseline SINR, similar to Baseline RSRP, leverages the eGA proposed in Section V, but its designed to maximize the following objective function:

$$\text{Obj}^{\text{eGA}}_{\text{bl,rsrp}} := \min\Big(\Big\{\mathbb{E}_{\tau,\mathbf{h}^{\text{dl}}}\Big\{\gamma^{\text{ssb}}_{r}(\mathbf{X},\mathbf{P})\Big\} \mid \forall r \in \mathbf{r}_{\text{AH}}\Big\}\Big). \tag{54}$$

In this configuration, the SSBs beams and power configurations are selected among all the cells in the network to maximize the SSB SINR coverage on the AH; differently from our proposed solution, in this scenario, the solution is searched among all cells without any constraints derived from the optimal AH split and serving cell selection.

A. SINR AND ACHIEVABLE DATA RATE

Within the specified network configuration, a linear AH spanning 1250 m is placed across several cell boundaries. Along this AH, 12 flying UAVs are evenly deployed maintaining a minimum distance of 100 m between each other [62]. The AH itself is situated at an altitude of 100 m. In this scenario, an average of 4 gUEs are considered per cell, resulting in a total of 228 gUEs within the network. Utilizing this setup, our solution delineates six distinct segments along the AH, identifying the optimal serving cell for each segment and selecting the best SSB beams from each cell to facilitate the desired UAV-to-cell associations.

Figure 5 shows results in terms of SINR and achievable data rate distributions. Compared to the baselines, our solution demonstrates significant improvements in SINR and data rate performance. Specifically, it achieves SINR values of −2.06 dB and 3.78 dB for the 5%-tile and the mean,

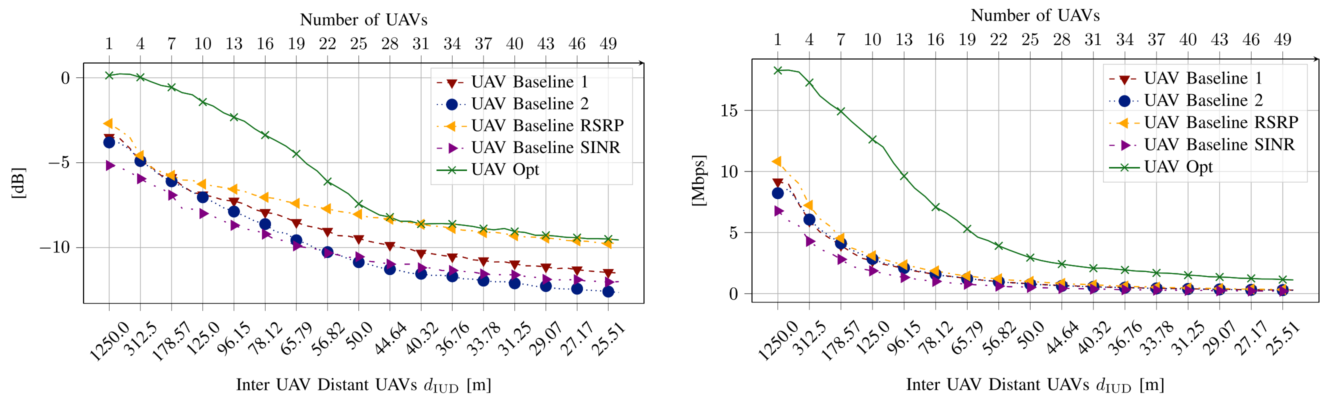

(a) Evolution of the 5%-tile UAVs SINR (b) Evolution of the 5%-tile UAVs Achievable Data Rate

FIGURE 6. **UAVs 5%-tile SINR (Figure 6(a)) and achievable data rate (Figure 6(b)) evolution for different number of equally-spaced UAVs and respective d_{IUD} over a 1250 m straight aerial highway positioned across cell edges at 100 m height.**

TABLE 4. **Summary of results for UAVs SINR and achievable data rate.**

	UAVs KPI			
	SINR [dB]		**Rate** [Mbps]	
	5%-tile	**Mean**	**5%-tile**	**Mean**
Baseline 1	-7.21	-1.50	2	12
Baseline 2	-7.66	-0.89	2	15
Baseline RSRP	-6.47	-1.59	3	10
Baseline SINR	-8.44	-0.82	1	15
Opt	**-2.06**	**3.78**	**11**	**32**

respectively, translating to gains of 5.15 dB and 5.21 dB over Baseline 1, and 5.59 dB and 4.66 dB over Baseline 2. While, considering Baseline RSRP and Baseline SINR, our solution introduce a gain for the 5%-tile and the mean value, respectively, of 4.40 dB and 5.37 dB over Baseline RSRP and 6.38 dB and 4.60 dB against Baseline SINR. In terms of data rates, our solution attains 11 Mbps and 32 Mbps for the 5%-tile and mean values, respectively. This marks a substantial enhancement over Baseline 1 (2 Mbps and 12 Mbps), Baseline 2 (2 Mbps and 15 Mbps), Baseline RSRP (3 Mbps and 10 Mbps), Baseline SINR (1 Mbps and 15 Mbps). Translating those improvements in percentage gains, our proposed solution introduce the following gains for, respectively, the 5%-tile and mean of UAVs achievable data rate: 550 %, 266 % against Baseline 1, 550 %, 213 % over Baseline 2, 366 %, 320 % against Baseline RSRP and 1100 %, 213 % over Baseline SINR.

Table 4 summarizes the results presented above.

Moreover, considering an SINR outage threshold of -6 dB, Baselines 1 and 2 show, respectively, outage rates of 10.07 % and 10.56 %, while Baseline RSRP and SINR exhibit rate of 6.97% and 11.96%. It is important to note that, in contrast with that, our solution lowers this rate to 0.59%.

B. TRAFFIC ANALYSIS

To delve deeper into the advantages of our proposed solution, we explore the impact of increased traffic on the AH on UAVs' SINR and achievable data rates, particularly focusing on the 5%-tile values. Leveraging the scenario outlined in Section VI-A, we scale the number of UAVs navigating the AH up to 50. Consistent with Section II, these UAVs maintain a fixed distance apart, denoted as d_{IUD}, which we are going to vary to increase traffic. Figure 6 illustrates the evolution of the 5%-tile values for SINR and achievable data rates as traffic increases. Our analysis confirms that our solution consistently surpasses the baselines in terms of maintaining robust, high-quality connectivity on the AH, irrespective of traffic density. With a minimum SINR threshold of -6 dB for the 5%-tile, Baseline 1, Baseline 2, Baseline RSRP and Baseline SINR support a maximum of 7, 6, 7 and 4 UAVs, respectively, whereas our solution can support up to 21 UAVs. This effectively triples, or even quintuples, the traffic capacity on the AH, with similar benefits observed in data rate performance. The improvement stems from the strategic selection of serving cells, which exhibit a rich diversity in angles of arrival/departure AoAs/AoDs. This diversity increases signal qualities and spatial multiplexing capabilities, leading to larger achievable data rates. The observed decline in SINR in Figure 6(a) primarily results from increased interference due to the use of more distinct data beams to serve UAVs. The inflection point in such figure indicates the point beyond which no additional data beams are activated, thereby changing the rate at which interference increases. This saturation also affects data rate trends, albeit less markedly. At lower UAV counts, SINR variations predominantly drive the negative data rate slope. Beyond the saturation point, the limited ability to further spatially multiplex closely positioned UAVs on the same PRBs results in a decline in data rates performance. Furthermore, it should be noted that, while considering increasing traffic conditions, among all the considered baselines, Baseline SINR appears to be the worst performing in terms of data rate. Optimizing solely for coverage SINR can result in a situation where the cells can provide excellent coverage signal quality but are inefficient at multiplexing UAVs during the data precoding phase, thereby resulting in significantly reduced data rate performance.

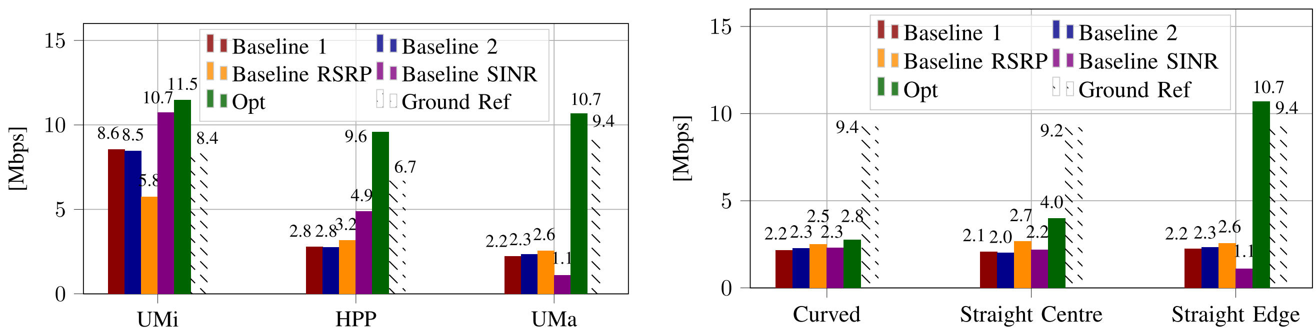

(a) Different Network Layout 5%-tile UAVs Achievable Data Rate (b) Different AH Configuration 5%-tile UAVs Achievable Data Rate

FIGURE 7. Comparison of UAVs 5%-tile achievable data rates for different urban scenarios (Figure 7(a)) and different AH configurations (Figure 7(b)).

C. DIFFERENT NETWORK LAYOUT ANALYSIS

In this analysis, we explore the performance of UAVs in terms of their achievable data rates across different network layouts. We particularly focus on the 5%-tile of performance to highlight the worst-case scenarios for UAVs. The outcomes from Section VI-A, referred to as the UMa scenario, are compared against two additional configurations: the UMi scenario, featuring tri-sectorized sites in a 2-tier hexagonal grid with inter-site distance (ISD) of 200 m and base station (BS) heights of 10 m, and the Urban Random Distributed (URD) scenario, with tri-sectorized sites randomly placed, ensuring an ISD of at least 200 m and base station heights of 25 m. It should be noted that for the URD scenario, the channel model parameters are equivalent to those of the UMa. The same AH and UAV traffic setup from Section VI-A is maintained for consistency.

Figure 7(a) showcases the results, highlighting that our proposed solution consistently surpasses baselines performances across all urban scenarios. It is noteworthy, however, that the performance gains in the UMi scenario are diminished. This reduction in gains can be attributed to the UMi‘s denser environment, which shortens distances and LoS probabilities, consequently enhancing the AoAs/AoDs diversity across all cells and diminishing the distinction between optimal and suboptimal serving cells. Additionally, the elevated path loss exponent inherent to the UMi scenario naturally curtails interference, thereby somewhat negating the advantages of our cell selection strategy. In the URD scenario, the unpredictable nature of site deployments potentially restricts the choice of serving cells (in some cases to no more than one sector per AH segment), thereby capping the gains.

A key takeaway from this analysis is that while gains are somewhat moderate due to the overlapping characteristics of serving cells identified by our solution and those in the baseline scenarios, this overlap with baselines arises from random and uncontrolled environmental factors, thus lacking reliability. Conversely, our approach provides a systematic and robust method for selecting optimal serving cells across various urban layouts, thereby enhancing the lower bounds of UAV performance.

D. DIFFERENT AERIAL HIGHWAY CONFIGURATION ANALYSIS

The analysis focuses on comparing the 5%-tile of UAVs data rate under different AH configurations, specifically considering variations in AH trajectories and positions. We compare results in Section VI-A, here referred as “Straight Edges” with two alternative AHs: “Curved”, which spans from the bottom right to the top left of the network layout, and “Straight Centres”, a linear trajectory from the network’s bottom to its top, deliberately aligned to pass above base station sites. Unlike “Straight Edges”, “Straight Centres” is adjusted to frequently traverse the central areas of cells.

Figure 7(b) illustrates the findings from these scenarios. Across all configurations, the proposed solution demonstrates superior performance compared to the baselines. Nonetheless, the “Curved” and “Straight Centres” scenarios exhibit diminished gains. This outcome stems from the inherent challenges in distinguishing optimal serving cells when the AH navigates closer to network centres, where the AH‘s positioning relative to the network and its inherent configuration–factors beyond the network operator’s control–tend to increase the AoAs/AoDs diversity and average channel gains. Consequently, the advantage of selecting diverse serving cells is less pronounced. Our methodology consistently ensures optimal serving cell selection, improving UAVs performance regardless of the AH‘s trajectory or network configuration. This highlights the robustness of our solution in enhancing UAVs connectivity across various operational contexts.

VII. CONCLUSION

In this paper, we proposed a novel solution for supporting mMIMO connectivity for UAVs over pre-defined aerial highways without affecting the performance of terrestrial users. Specifically, we investigated how solely controlling the UAV serving cells by optimally planning the SSB beams that govern cell association is the key to boosting UAV data rates and reliability. To tackle this, we formulated an optimization problem to select, from a fixed codebook, the optimal combination of SSB beams and transmission power to be deployed within the network. To solve this NP-Hard problem, we devised a heuristic approach based on a novel metric, namely MAMA, aimed to select the optimal set of cells to serve the aerial highway. This metric exploits the a-priori information of the aerial highway to capture and blend information about spatial diversity, average channel gains, and interference. Our heuristic solution, leveraging this metric, divided the problem into two less complex sub-problems. First, the aerial highway is optimally split into multiple segments, and the set of serving cells is defined. Then, the optimal combination of SSB beams and transmitting power is determined to ensure optimal coverage from the defined serving cells.

Our results demonstrate the efficacy of our approach of optimally controlling UAVs association, with UAVs experiencing gains exceeding 5 dB in the 5%-tile SINR and a five-fold increase in the 5%-tile achievable data rate. Additionally, our findings highlight that relying on traditional coverage methods, such as blindly maximizing AH‘s RSRP or SINR without intelligent serving cell selection, may limit UAVs data rate performance. This underscores the necessity for additional metrics, such as the proposed MAMA metric, to select AH‘s serving cells optimally and, in turn, provide optimal coverage from those and maximize UAVs data rate.

Future work will extend our research by integrating and delving into mobility-related challenges, as well as integrating privacy and security aspects, crucially for cellular-connected UAVs within the urban environment.

APPENDIX

In the following, we provide a detailed description of the acLoS probability and path loss gain models. Additionally, Table 5 lists the key notations used in this work.

TABLE 5. Key notation list.

Name	Description
d_{ISD}	Inter-site distance
$\mathcal{B}$	Set of all sectors/cells
N_{BS}	Number of all sectors/cells
M_h, M_v	Panel horizontal and vertical antennas
M	Panel total number of antenna
N_u	Total number of UEs
N_g, N_a	Total number of gUEs, UAVs
$\mathcal{U}, \mathcal{U}_b$	Set of all UEs, set of UEs associated with cell b
d_{IUD}	Inter-UAVs distance on AH
$d^{\text{2D}}_{u,b}, d^{\text{3D}}_{u,b}$	2D, 3D distances
$\phi_{u,b}, \theta_{u,b}$	Azimuth, zenith angles
$P^{\text{UMa-LoS}}_{u,b}, P^{\text{UMi-LoS}}_{u,b}$	LoS probabilities
$\rho_{u,b}$	Path loss gain
$g_{u,b}, \tau_{u,b}$	Antenna element and shadow fading gain
$\beta_{u,b}$	Large-scale channel gain
$\mathbf{V}_b$	Panel antenna cartesian coordinates
$\mathbf{h}^{\text{dl}}_{u,b}$	Downlink small-scale channel vector
$\mathbf{w}^{\text{ssb}}_{s,b}, \mathbf{W}^{\text{ssb}}$	SSB codeword and codebook
N_{ssb}	Number of SSB beams at each cell
N_{CB}	Total number of SSB codeword
$\mathbf{p}^{\text{ssb}}_{s,b}, \mathbf{p}^{\text{ssb}}_{\max}$	SSB power and maximum power
$\mathbf{X}$	Network transmitted SSB binary matrix
$\mathbf{P}$	Network transmitted SSB power matrix
$\mathbf{X}^{\text{bl}}, \mathbf{P}^{bl}$	Baseline conf. SSB binary matrices
$\text{rsrp}^{\text{ssb}}_{u,s,b}$	SSB measured RSRP
$\hat{s}_u, \hat{b}_u$	Serving SSB index, serving cell
γ^{ssb}_u	Coverage SSB SINR
$\mathbf{w}^{\text{csi-rs}}_{\text{pmi}}$	CSI-RS codeword
$\mathbf{w}^{\text{dl}}_{u,b}, p^{\text{dl}}_{u,b}$	UE’s downlink data codeword and power
$\mathbf{W}^{\text{dl}}_b$	Codebook of all UEs data codeword
$N_{\mathbf{w}^{\text{dl}}_{u,b}}$	UE’s number served by same codeword
γ_u, R_u	UEs SINR and achievable data rate
R_g, R_a	gUEs, UAVs achievable data rate
$\mathbf{r}_{\text{AH}}, \mathbf{z}$	AH Discrete Points and AH’s segment
N_r, N_z	Number of AH and Segment’s Discrete Points
$\tilde{\mathbf{H}}_{\mathbf{r},b}, \tilde{\mathbf{H}}_{\mathbf{z},b}$	AH and segment exp. complex channel matrix
$\tilde{\mathbf{H}}_{\mathbf{r}-\mathbf{z},b}$	AH’s w/o segment exp. complex channel matrix
$\chi_{\mathbf{z},b}$	MAMA Metric
$P_{\mathbf{z},b}, c_{\mathbf{z},b}$	Average Channel Gain, inv. condition number
$F_{\mathbf{z},b}$	Squared Frobenious Norm
$\boldsymbol{\lambda}_{\mathbf{z},b}$	Set of ordered singular values
$\mathcal{Z}_{\text{AH}}$	Set of AH’s segments
$\hat{b}_{\mathbf{z}}, \mathbf{b}^{\text{split}}_{\mathbf{z}}$	Seg. $\mathbf{z}$ serving cell and set of serving cells
$N^{\min}_{\text{seg}}, N^{\max}_{\text{seg}}$	Minimum, Maximum number of Segments
$\mathbf{x}^{(p)}, \mathbf{v}^{(p)}$	PSO particle p position and velocity
$\mathbf{z}^{(p)}_n$	PSO particle p obtained segment
w, ϕ_c, ϕ_s	PSO inertia, cognitive, social Coeff.
$c1, c2$	Uniform random numbers
$\mathbf{x}^{(p)}_{\text{best}}, \mathbf{x}_{\text{best}}$	PSO particle p best and global best position
$\mathcal{Z}^{\text{split}}, \mathbf{b}^{\text{split}}_{\mathbf{z}}$	PSO resulting set of segments and serving cells
$N^{\text{Iter}}_{\text{pso}}, N_{\text{swarm}}$	PSO number of iterations and particles
$M^{(i)}_h$	Conf. i-th number of horizontal active antenna
$\mathbf{W}^{(i)}, \mathbf{F}_{M,M^{(i)}}$	Conf. i-th SSB codebook, codeword mapping
$\mathbf{y}^{(q)}$	eGA individual q
$s^{(q)}_{\hat{b}_{\mathbf{z}}}, p^{\text{ssb}\,(q)}_{\hat{b}_{\mathbf{z}}}$	Individual q SSB index and power at cell $\hat{\mathbf{b}}_{\mathbf{z}}$
$N_{\text{pop}}, N^{\text{Iter}}_{\text{eGA}}$	eGA number of iteration and individuals
$P_{\text{cross}}, P_{\text{mut}}$	eGA crossover, mutation probabilities
N_p, N_e	eGA number of parents and elites

A. LOS PROBABILITY AND PATH LOSS GAIN

In the following, we report the adopted models outlined by 3GPP in [44], [45] for LoS probability $P^{\text{LoS}}_{u,b}$ and path loss gain $\rho_{u,b}$ between each UEs u and each cell b; both considering UMa, UMi scenarios as well as UEs located on the ground segment and UAVs on the aerial one. Here, distances and frequencies are expressed in meters and GHz.

UMa Ground Segment: Following models presented in [44], we consider a UMa scenario with outdoor gUE at a fixed altitude h_g of 1.5 m. Between each gUE g and cell b the LoS probability $P^{\text{LoS}}_{g,b}$ is computed as follows,

$$P^{\text{LoS}}_{g,b} = \begin{cases} 1, & \text{If } d^{\text{2D}}_{g,b} \leq 18\text{m} \\ \left[\frac{18}{d^{\text{2D}}_{g,b}} + e^{-\frac{d^{\text{2D}}_{g,b}}{63}}\left(1 - \frac{18}{d^{\text{2D}}_{g,b}}\right)\right], & \text{Otherwise} \end{cases}, \quad (55)$$

where $d^{\text{2D}}_{g,b}$ is the 2D distance between gUE g and cell b. Following this, we compute, for both LoS and not line of sight (NLoS) scenario, the path loss gain in dB $\rho^{\text{UMa-LoS, dB}}_{g,b}$ and $\rho^{\text{UMa-NLoS, dB}}_{g,b}$ as follows,

$$\rho^{\text{UMa-LoS, dB}}_{g,b} = \begin{cases} -PL^{\text{UMa-LoS, dB}}_1, & \text{If } 10\text{m} \leq d^{\text{2D}}_{g,b} \leq d_{\text{BP}} \\ -PL^{\text{UMa-LoS, dB}}_2, & \text{If } d_{\text{BP}} \leq d^{\text{2D}}_{g,b} \leq 5\text{km} \end{cases}, \quad (56)$$

where

$$PL_1^{\text{UMa-LoS, dB}} = 28.0 + 22\log_{10}\left(d_{g,b}^{3D}\right) + 20\log_{10}(f_c) \quad (57)$$

$$PL_2^{\text{UMa-LoS, dB}} = 28.0 + 40\log_{10}\left(d_{g,b}^{3D}\right) + 20\log_{10}(f_c) - 9\log_{10}\left(d_{\text{BP}}^2 + \left(h_{\text{BS}} - h_g\right)^2\right), \quad (58)$$

and

$$\rho_{g,b}^{\text{UMa-NLoS, dB}} = \min\left(\rho_{g,b}^{\text{UMa-LoS, dB}}, -PL^{\text{UMa-NLoS, dB}}\right), \quad (59)$$

$$PL^{\text{UMa-NLoS, dB}} = 13.54 + 39.08\log_{10}\left(d_{g,b}^{3D}\right) + 20\log_{10}(f_c) - 0.6\left(h_g - 1, 5\right), \quad (60)$$

where $d_{g,b}^{3D}$ is 3D distances between gUE g and cell b, and d_{BP} is the breakpoint distance computed as in [44],

$$d_{\text{BP}} = \frac{4(h_{\text{BS}} - 1)\left(h_g - 1\right)f_c}{c}, \quad (61)$$

where c is the speed of light.

UMi Ground Segment: Here, we present the adopted model for outdoor gUEs in a UMi scenario. Following models in [44], the LoS probability $P_{g,b}^{\text{LoS}}$ in this scenario is computed as in eq. (55). Differently, the path loss gains in dB $\rho_{g,b}^{\text{LoS, dB}}$, $\rho_{g,b}^{\text{NLoS, dB}}$ are computed according to the following models,

$$\rho_{g,b}^{\text{UMi-LoS, dB}} = \begin{cases} -PL_1^{\text{UMi-LoS, dB}}, & \text{If } 10\text{m} \le d_{g,b}^{2D} \le d_{\text{BP}} \\ -PL_2^{\text{UMi-LoS, dB}}, & \text{If } d_{\text{BP}} \le d_{g,b}^{2D} \le 5\text{km} \end{cases}, \quad (62)$$

where

$$PL_1^{\text{UMi-LoS, dB}} = 32.4 + 21\log_{10}\left(d_{g,b}^{3D}\right) + 20\log_{10}(f_c), \quad (63)$$

$$PL_2^{\text{UMi-LoS, dB}} = 32.4 + 40\log_{10}\left(d_{g,b}^{3D}\right) + 20\log_{10}(f_c) - 9.5\log_{10}\left(d_{\text{BP}}^2 + \left(h_{\text{BS}} - h_g\right)^2\right), \quad (64)$$

with d_{BP} computed as in eq. (61).

UMa Aerial Segment: In the following, we introduce the adopted models for UAVs outlined in [45] for a UMa scenario. Between each UAVs a and cell b, the LoS probability $P_{a,b}^{UMa-LoS}$ is computed as follows,

$$P_{a,b}^{UMa-LoS} = \begin{cases} 1, & \text{If } 100\text{m} < h_{\text{AH}} \le 300\text{m} \\ p_1^{\text{UMa}}, & \text{Otherwise} \end{cases}, \quad (65)$$

with

$$p_1 = \begin{cases} 1, & \text{If } d_{a,b}^{2D} \le d_1^{\text{UMa}} \\ \frac{d_1^{\text{UMa}}}{d_{a,b}^{2D}} + e^{-\frac{d_{a,b}^{2D}}{\bar{p}_1^{\text{UMa}}}}\left(1 - \frac{d_1^{\text{UMa}}}{d_{a,b}^{2D}}\right), & \text{Otherwise} \end{cases}, \quad (66)$$

and

$$\bar{p}_1^{\text{UMa}} = 4300\log_{10}(h_{\text{AH}}) - 3800, \quad (67)$$

$$d_1^{\text{UMa}} = \max\left(460\log_{10}(h_{\text{AH}}) - 700, 18\right). \quad (68)$$

Then, we compute the path loss gain in dB as follows,

$$\rho_{a,b}^{\text{UMa-LoS, dB}} = -28.0 - 22\log_{10}\left(d_{a,b}^{3D}\right) - 20\log_{10}(f_c) \quad (69)$$

$$\rho_{a,b}^{\text{UMa-NLoS, dB}} = +17.5 - 20\log_{10}\left(\frac{40\pi f_c}{3}\right) - \left(46 - 7\log_{10}(h_{\text{AH}})\right)\log_{10}\left(d_{a,b}^{3D}\right). \quad (70)$$

UMi Aerial Segment: Here, we present the adopted model for outdoor UAVs in a UMi scenario. Following models in [45], the LoS probability $P_{a,b}^{\text{UMi-LoS}}$ is computed as follows,

$$P_{a,b}^{\text{UMi-LoS}} = \begin{cases} 1, & \text{If } d_{a,b}^{2D} \le d_1^{\text{UMi}} \\ \frac{d_1^{\text{UMi}}}{d_{a,b}^{2D}} + e^{-\frac{d_{a,b}^{2D}}{\bar{p}_1^{\text{UMi}}}}\left(1 - \frac{d_1^{\text{UMi}}}{d_{a,b}^{2D}}\right), & \text{Otherwise} \end{cases}, \quad (71)$$

where

$$\bar{p}_1^{\text{UMi}} = 233.98\log_{10}(h_{\text{AH}}) - 0.95, \quad (72)$$

$$d_1^{\text{UMi}} = \max\left(294.05\log_{10}(h_{\text{AH}}) - 432.94, 18\right). \quad (73)$$

Then, we compute the path loss gains in dB for the UMi scenario as follows,

$$\rho_{a,b}^{\text{UMi-LoS, dB}} = \min\begin{cases} -30.9 - \left(22.25 - 0.5\log_{10}(h_{\text{AH}})\right)\log_{10}\left(d_{a,b}^{3D}\right) \\ -20\log_{10}(f_c) \\ -\text{FS}_{a,b} \end{cases}, \quad (74)$$

$$\rho_{a,b}^{\text{UMi-NLoS, dB}} = \min\begin{cases} -32.4 - \left(43.42 - 7.6\log_{10}(h_{\text{AH}})\right)\log_{10}\left(d_{a,b}^{3D}\right) \\ -20\log_{10}(f_c) \\ \rho_{a,b}^{\text{UMi-LoS, dB}} \end{cases}, \quad (75)$$

where FS is the free space path loss computed as follows,

$$\text{FS}_{a,b} = 32.45 + 20\log_{10}\left(d_{a,b}^{3D}\right) + 20\log_{10}(f_c). \quad (76)$$

In the rest of the paper, to simplify notation, we refer to the path loss gain in linear scale, between UE u and cell b, with $\rho_{u,b}$.

REFERENCES

[1] A. Fotouhi et al., "Survey on UAV cellular communications: Practical aspects, standardization advancements, regulation, and security challenges," *IEEE Commun. Surveys Tuts.*, vol. 21, no. 4, pp. 3417–3442, Mar. 2019.

[2] B. Li, Z. Fei, and Y. Zhang, "UAV communications for 5G and beyond: Recent advances and future trends," *IEEE Internet Things J.*, vol. 6, no. 2, pp. 2241–2263, Apr. 2019.

[3] S. Wang, L. Yang, X. Li, K. Guo, H. Liu, H. Song, and R. H. Jhaveri, "Performance analysis of satellite-vehicle networks with a non-terrestrial vehicle," *IEEE Trans. Intell. Veh.*, vol. 9, no. 1, pp. 1691–1700, Jun. 2024.

[4] M. Mozaffari, W. Saad, M. Bennis, Y.-H. Nam, and M. Debbah, "A tutorial on UAVs for wireless networks: Applications, challenges, and open problems," *IEEE Commun. Surveys Tuts.*, vol. 21, no. 3, pp. 2334–2360, Mar. 2019.

[5] G. Geraci et al., "What will the future of UAV cellular communications be? A flight from 5G to 6G," *IEEE Commun. Surveys Tuts.*, vol. 24, no. 3, pp. 1304–1335, 3rd Quart., 2022.

[6] S. Li, L. Yang, D. B. da Costa, and S. Yu, "Performance analysis of UAV-based mixed RF-UWOC transmission systems," *IEEE Trans. Commun.*, vol. 69, no. 8, pp. 5559–5572, May 2021.
[7] E. Vinogradov, H. Sallouha, S. De Bast, M. M. Azari, and S. Pollin, "Tutorial on UAV: A blue sky view on wireless communication," 2019, *arXiv:1901.02306*.
[8] S. Qi, B. Lin, Y. Deng, X. Chen, and Y. Fang, "Minimizing maximum latency of task offloading for multi-UAV-assisted maritime search and rescue," *IEEE Trans. Veh. Technol.*, early access, Apr. 3, 2024, doi: 10.1109/TVT.2024.3384570.
[9] H. Kong, M. Lin, L. Han, W.-P. Zhu, Z. Ding, and M.-S. Alouini, "Uplink multiple access with semi-grant-free transmission in integrated satellite-aerial-terrestrial networks," *IEEE J. Sel. Areas Commun.*, vol. 41, no. 6, pp. 1723–1736, May 2023.
[10] Y. Zeng, Q. Wu, and R. Zhang, "Accessing from the sky: A tutorial on UAV communications for 5G and beyond," *Proc. IEEE*, vol. 107, no. 12, pp. 2327–2375, Dec. 2019.
[11] (Market Growth Reports, Pune, Maharashtra). *Global Civil Drone Industry Research Report 2023, Competitive Landscape, Market Size, Regional Status and Prospect*. Jan. 2023.
[12] (Bus. Res. Company, London, U.K.). *Commercial Drones Global Market Report 2023*. Jan. 2023.
[13] (New York Times, New York, NY, USA). *Drone Delivery? Amazon Moves Closer With F.A.A. Approval*. Aug. 2020.
[14] (Amazon, Seattle, WA, USA). *Amazon is Launching Ultra-Fast Drone Deliveries in Italy, the U.K., and a Third Location in the U.S.*. Oct. 2023.
[15] (Times, Mumbai, Maharashtra). *Amazon Prime Delivery Drones to Take Flight in the U.K. Next Year*. Oct. 2023.
[16] N. Cherif, W. Jaafar, H. Yanikomeroglu, and A. Yongacoglu, "3D aerial highway: The key enabler of the retail industry transformation," *IEEE Commun. Mag.*, vol. 59, no. 9, pp. 65–71, Sep. 2021.
[17] V. Marojevic, I. Guvenc, R. Dutta, M. L. Sichitiu, and B. A. Floyd, "Advanced wireless for unmanned aerial systems: 5G standardization, research challenges, and AERPAW architecture," *IEEE Veh. Technol. Mag.*, vol. 15, no. 2, pp. 22–30, Apr. 2020.
[18] D. López-Pérez et al., "On the downlink performance of UAV communications in dense cellular networks," in *Proc. IEEE Global Commun. Conf. (GLOBECOM)*, 2018, pp. 1–7.
[19] Z. Wang, M. Lin, J. Ouyang, J.-B. Wang, W.-P. Zhu, and N. Al-Dhahir, "Multi-objective robust beamforming for integrated satellite and aerial networks supporting heterogeneous services," *IEEE Trans. Wireless Commun.*, vol. 22, no. 10, pp. 6870–6882, Feb. 2023.
[20] X. Lin et al., "The sky is not the limit: LTE for unmanned aerial vehicles," *IEEE Commun. Mag.*, vol. 56, no. 4, pp. 204–210, Apr. 2018.
[21] R. Muzaffar, C. Raffelsberger, A. Fakhreddine, J. L. Luque, D. Emini, and C. Bettstetter, "First experiments with a 5G-connected drone," in *Proc. 5th Workshop Micro Aerial Veh. Net., Syst., Appl.*, 2020, pp. 1–5.
[22] D. Gesbert, M. Shafi, D. shan Shiu, P. Smith, and A. Naguib, "From theory to practice: An overview of MIMO space-time coded wireless systems," *IEEE J. Sel. Areas Commun.*, vol. 21, no. 3, pp. 281–302, Apr. 2003.
[23] A. Goldsmith, S. Jafar, N. Jindal, and S. Vishwanath, "Capacity limits of MIMO channels," *IEEE J. Sel. Areas Commun.*, vol. 21, no. 5, pp. 684–702, Jun. 2003.
[24] D. Gesbert, H. Bolcskei, D. Gore, and A. Paulraj, "Outdoor MIMO wireless channels: Models and performance prediction," *IEEE Trans. Commun.*, vol. 50, no. 12, pp. 1926–1934, Dec. 2002.
[25] M. Wu, K. Guo, Z. Lin, X. Li, K. An, and Y. Huang, "Joint optimization design of RIS-assisted hybrid FSO SAGINs using deep reinforcement learning," *IEEE Trans. Veh. Technol.*, vol. 73, no. 3, pp. 3025–3040, Oct. 2024.
[26] M. Wu et al., "Deep reinforcement learning-based energy efficiency optimization for RIS-aided integrated satellite-aerial-terrestrial relay networks," *IEEE Trans. Commun.*, early access, Feb. 26, 2024, doi: 10.1109/TCOMM.2024.3370618.
[27] N. Cherif, W. Jaafar, H. Yanikomeroglu, and A. Yongacoglu, "Disconnectivity-aware energy-efficient cargo-UAV trajectory planning with minimum handoffs," in *Proc. IEEE Int. Conf. Comm. (ICC)*, 2021, pp. 1–6.
[28] O. Esrafilian, R. Gangula, and D. Gesbert, "Three-dimensional-map-based trajectory design in UAV-aided wireless localization systems," *IEEE Internet Things J.*, vol. 8, no. 12, pp. 9894–9904, Sep. 2021.
[29] U. Challita, W. Saad, and C. Bettstetter, "Deep reinforcement learning for interference-aware path planning of cellular-connected UAVs," in *Proc. IEEE Int. Conf. Comm. (ICC)*, 2018, pp. 1–6.
[30] S. De Bast, E. Vinogradov, and S. Pollin, "Cellular coverage-aware path planning for UAVs," in *Proc. IEEE Workshop Signal Process. Adv. Wireless Commun. (SPAWC)*, 2019, pp. 1–5.
[31] O. Esrafilian, R. Gangula, and D. Gesbert, "3D-map assisted UAV trajectory design under cellular connectivity constraints," in *Proc. IEEE Int. Conf. Comm. (ICC)*, 2020, pp. 1–6.
[32] A. Colpaert, M. Raes, E. Vinogradov, and S. Pollin, "Drone delivery: Reliable cellular UAV communication using multi-operator diversity," in *Proc. IEEE Int. Conf. Comm. (ICC)*, 2022, pp. 1–6.
[33] R. Amorim, I. Z. Kovacs, J. Wigard, G. Pocovi, T. B. Sorensen, and P. Mogensen, "Improving drone's command and control link reliability through dual-network connectivity," in *Proc. IEEE Veh. Tech. Conf. (VTC)*, 2019, pp. 1–6.
[34] J. Säe, R. Wirén, J. Kauppi, J. Torsner, S. Andreev, and M. Valkama, "Reliability of UAV connectivity in dual-MNO networks: A performance measurement campaign," in *Proc. IEEE Int. Conf. Comm. (ICC)*, 2020, pp. 1–5.
[35] A. Bhuyan, I. Guvenc, H. Dai, Y. Yapici, A. Rahmati, and S. J. Maeng, "Secure mmwave cellular network for drone communication," in *Proc. IEEE Veh. Tech. Conf. (VTC)*, 2019, pp. 1–5.
[36] A. Bhuyan et al., "Secure 5G network for a nationwide drone corridor," in *Proc. IEEE Aerosp. Conf. (AeroConf)*, 2021, pp. 1–10.
[37] S. J. Maeng, M. M. U. Chowdhury, I. Güvenç, A. Bhuyan, and H. Dai, "Base station antenna uptilt optimization for cellular-connected drone corridors," *IEEE Trans. Aerosp. Elect. Syst.*, vol. 59, no. 4, pp. 4729–4737, Jan. 2023.
[38] S. Karimi-Bidhendi, G. Geraci, and H. Jafarkhani, "Optimizing cellular networks for UAV corridors via quantization theory," 2023, *arXiv:2308.01440*.
[39] M. Benzaghta, G. Geraci, D. López-Pérez, and A. Valcarce, "Designing cellular networks for UAV corridors via Bayesian optimization," in *Proc. IEEE Global Commun. Conf. (GLOBECOM)*, 2023, pp. 4552–4557.
[40] Y. Huang, Q. Wu, R. Lu, X. Peng, and R. Zhang, "Massive MIMO for cellular-connected UAV: Challenges and promising solutions," *IEEE Commun. Mag.*, vol. 59, no. 2, pp. 84–90, Feb. 2021.
[41] A. Garcia-Rodriguez, G. Geraci, D. Lopez-Perez, L. G. Giordano, M. Ding, and E. Bjornson, "The essential guide to realizing 5G-connected UAVs with massive MIMO," *IEEE Commun. Mag.*, vol. 57, no. 12, pp. 84–90, Oct. 2019.
[42] G. Geraci, A. Garcia-Rodriguez, L. Galati Giordano, D. López-Pérez, and E. Björnson, "Understanding UAV cellular communications: From existing networks to massive MIMO," *IEEE Access*, vol. 6, pp. 67853–67865, 2018.
[43] M. Bernabè, D. López-Pérez, N. Piovesan, G. Geraci, and D. Gesbert, "A novel metric for mMIMO base station association for aerial highway systems," in *Proc. IEEE Int. Conf. Comm. (ICC)*, 2023, pp. 1063–1068.
[44] "Study on channel model for frequencies from 0.5 to 100 GHz; (Release 16), Version 14.0," 3GPP Sophia Antipolis, France, Rep. TR 38.901, Mar. 2017.
[45] "Enhanced LTE support for aerial vehicles; (Release 15), Version 15.0," 3GPP Sophia Antipolis, France, Rep. TR 36.777, Jan. 2017.
[46] X. Cai and G. Giannakis, "A two-dimensional channel simulation model for shadowing processes," *IEEE Trans. Veh. Technol.*, vol. 52, no. 6, pp. 1558–1567, Nov. 2003.
[47] E. Björnson, J. Hoydis, and L. Sanguinetti, "Massive MIMO networks: Spectral, energy, and hardware efficiency," *Found. Trends® Signal Process.*, vol. 11, nos. 3–4, pp. 154–655, 2017.
[48] NR and NG-RAN overall description; (Release 15), Version 17.6, 3GPP Sophia Antipolis, France, Rep. TS 38.300, Sep. 2023.
[49] Physical channels and modulation; (Release 15), Version 18.0, 3GPP Sophia Antipolis, France, Rep. TS 38.211, Sep. 2023.
[50] E. Dahlman, S. Parkvall, and J. Skold, *5G NR: The Next Generation Wireless Access Technology*, 2nd ed. Waltham, MA, USA: Acad. Press, Inc., 2018.
[51] "Physical layer procedure for data; (Release 15), Version 18.0," 3GPP Sophia Antipolis, France, Rep. TR 38.214, Sep. 2023.
[52] D. A. Belsley, E. Kuh, and R. E. Welsch, *Regression Diagnostics: Identifying Influential Data and Sources of Collinearity*, 1st ed. New York, NY, USA: Wiley, 1980.

[53] J. Kennedy and R. Eberhart, "Particle swarm optimization," in *Proc. IEEE Int. Conf. Neural Net. (ICNN)*, 1995, pp. 1942–1948.
[54] Y. Shi and R. Eberhart, "A modified particle swarm optimizer," in *Proc. IEEE Int. Conf. Evol. Comp. Proc. (ICEC)*, 1998, pp. 69–73.
[55] A. P. Engelbrecht, *Computational Intelligence: An Introduction*, 2nd ed. New York, NY, USA: Wiley, 2007.
[56] J. H. Holland, "Genetic algorithms," *Sci. Am.*, vol. 267, no. 1, pp. 66–73, Jul. 1992.
[57] D. E. Goldberg and J. H. Holland, "Genetic algorithms and machine learning," *Mach. Learn.*, vol. 3, pp. 95–99, Oct. 1988.
[58] D. Bhandari, C. Murthy, and S. K. Pal, "Genetic algorithm with elitist model and its convergence," *Internat. J. Pattern Recognit. A.I.*, vol. 10, no. 6, pp. 731–747, Nov. 1996.
[59] M. Clerc and J. Kennedy, "The particle swarm-explosion, stability, and convergence in a multidimensional complex space," *IEEE Trans. Evol. Comput.*, vol. 6, no. 1, pp. 58–73, Feb. 2002.
[60] G. Rudolph, "Convergence analysis of canonical genetic algorithms," *IEEE Trans. Neural Netw.*, vol. 5, no. 1, pp. 96–101, Jan. 1994.
[61] A. E. Eiben, E. H. L. Aarts, and K. M. Van Hee, "Global convergence of genetic algorithms: A Markov chain analysis," in *Parallel Problem Solving from Nature*. Berlin, Germany: Springer, Jun. 1991, pp. 3–12.
[62] E. Vinogradov and S. Pollin, "Reducing safe UAV separation distances with U2U communication and new remote ID formats," in *Proc. IEEE Global Commun. Conf. Workshops (GLOBECOM Workshops)*, 2022, pp. 1425–1430.

ACRONYM

CSI-RS	channel state information-reference signal
SRS	sounding reference signal
P2P	point to point
UPA	uniform planar array
PMI	precoding matrix indicator
RI	rank indicator
CQI	channel quality indicator
DL	downlink
CDF	cumulative distribution function
DFT	discrete Fourier transform
2D-DFT	two dimensional discrete Fourier transform
NR	new radio
PL	path loss
AF	array factor
AH	aerial highway
PSO	particle swarm optimization
eGA	elite genetic algorithm
GA	genetic algorithm
ICC	international conference on communications
SSB	synchronization signal block
ES	Eigenscore
AoA	angle of arrival
AoD	angle of departure
UAV	unmanned aerial vehicle
CCUAV	cellular connected unmanned aerial vehicle
D2D	device to device
gUE	ground user equipment
UE	user equipment
MIMO	multiple-input multiple-output
mMIMO	massive multiple-input multiple-output
MU-mMIMO	multi-user massive multiple-input multiple-output
MU-MIMO	multi-user multiple-input multiple-output
SU-MIMO	single-user multiple-input multiple-output
PRB	physical resource block
RE	resource element
RSRP	reference signal received power
RSS	received signal strength
mmWave	millimetre wave
eICIC	enhanced inter-cell interference coordination
SINR	signal-to-interference-plus-noise ratio
UAM	urban air mobility
QoS	quality of services
UE	user equipment
LoS	line of sight
NLoS	not line of sight
BVLoS	beyond visual line of sight
DoF	degree of freedom
ZF	zero forcing
CSI	channel state information
3GPP	3rd Generation Partnership Project
SVD	single value decomposition
PBCH	physical broadcast channel
thp	throughput
UMi	urban micro
UMa	urban macro
CAGR	compound annual growth rate
HO	handover
MNO	mobile network operator
NOMA	non-orthogonal multiple access
BO	bayesan optimization
ML	machine learning
FR1	frequency range 1
SO	southern
E	eastern
NE	northeastern
RAN	radio access network
BS	base station
ISD	inter-site distance
IUD	inter-UAV distance
RRC	radio resource control
PSS	primary synchronization signal
SSS	secondary synchronization signal
PBCH	physical broadcasted channel
MINP	mixed-integer nonlinear problem
PAHSS	Particle Aerial Highway Swarm Segmentation
MAMA	mMIMO-Aerial-Metric-Association
URD	Urban Random Distributed
UDN	ultra dense network

MATTEO BERNABÈ (Student Member, IEEE) received the master's degree (cum laude) in telecommunication engineering from the University of Bologna in 2021. He is currently pursuing the Ph.D. degree with the Department of Communication Systems, EURECOM, Sophia Antipolis, France, and Huawei Technologies, Paris, France. His research interests include wireless systems, cellular-connected UAVs, massive MIMO, and large-scale network modelling and optimization.

DAVID LÓPEZ-PÉREZ (Senior Member, IEEE) is a Distinguished Researcher with Universitat Politecnica de Valencia. Before joining this position, he served as an Expert and Technical Leader with Huawei Technologies, Paris, and held the title of a Distinguished Member of Staff with Nokia Bell Labs, Dublin. He has pioneered work on cellular and Wi-Fi inter-working, explored multi-antenna capabilities, and investigated low-latency features for future indoor networks. He has authored a book on small cells and another on ultra-dense networks, in addition to publishing over 150 research manuscripts covering a variety of related topics. He is also a prominent inventor with 60+ patents. Throughout his career, he has focused on the study of both cellular and Wi-Fi networks, with primary research interests in network performance analysis, network planning and optimization, heterogeneous networks, non-terrestrial networks, green networking, machine learning, and the development of new technologies and features. His major contributions revolve around the understanding of small cells and ultra-dense networks, as well as advancements in data-driven modeling and optimization.

NICOLA PIOVESAN (Member, IEEE) received the Ph.D. degree in network engineering from the Polytechnic University of Catalonia, Barcelona, Spain, in 2020. He is a Senior Researcher with Huawei Technologies, Paris, France. His work focuses on large-scale network modeling, data-driven network optimization, green networking, and the integration of artificial intelligence in the telecom domain. He served as an Assistant Researcher with the Centre Tecnològic de Telecomunicacions de Catalunya, Barcelona, Spain, from 2016 to 2019. He was Awarded a Marie Skłodowska-Curie Fellowship by the European Commission in 2016. He has authored over 30 research articles and holds co-inventorship in over ten patent applications. His achievements have been recognized with the Huawei GTS President Award in 2021 and the Huawei Quality Star Award in 2024, acknowledging his successful research application into product development.

GIOVANNI GERACI (Senior Member, IEEE) is a Principal Research Scientist with Telefonica. He is also a tenured Associate Professor with Universitat Pompeu Fabra, Barcelona, where he served as the Head of Telecommunications Engineering. He was previously with Nokia Bell Labs and holds a dozen patents on wireless technologies. For his contributions to wireless communications, he received the IEEE Communications Theory Early Achievement Award in 2023, the IEEE ComSoc Outstanding Young Researcher Award for Europe, Middle East, and Africa in 2018, and the Best Paper Awards at IEEE Globecom in 2022 and PIMRC in 2019. He also served as an IEEE Distinguished Lecturer, as an Editor for the IEEE TRANSACTIONS ON WIRELESS COMMUNICATIONS and IEEE COMMUNICATIONS LETTERS, and as the chair of around 20 top-tier IEEE symposia and workshops.

DAVID GESBERT (Fellow, IEEE) received the Ph.D. degree from TelecomParis, France, in 1997. He is serving as the Director of EURECOM, Sophia Antipolis, France. From 1997 to 1999, he was with the Information Systems Laboratory, Stanford University. He was a Founding Engineer with Iospan Wireless Inc., a Stanford spin off pioneering MIMO-OFDM (currently Intel). Before joining EURECOM in 2004, he was with the Department of Informatics, University of Oslo. He has published about 350 articles and 25 patents, seven of them winning IEEE best paper awards. He has been the Technical Program Co-Chair for ICC2017 and has been named a Thomson-Reuters Highly Cited Researchers in computer science. He is a Board Member for the OpenAirInterface Software Alliance. He was a previous awardee of an ERC Advanced Grant in the area of future networks. In 2020, he was also awarded funding by the French Interdisciplinary Institute on Artificial Intelligence for a Chair in the area of AI for the future IoT. In 2021, he received the Grand Prix in Research jointly from IMT and the French Academy of Sciences.